Probing new physics with polarized τ and Λ_c in quasielastic $\nu_\tau + n \to \tau^- + \Lambda_c$ scattering process

Ya-Ru Kong,[1,*] Li-Fen Lai,[2,†] Xin-Qiang Li,[1,3,‡] Xin-Shuai Yan,[4,§] Ya-Dong Yang,[1,4,‖] and Dong-Hui Zheng[1,¶]

[1]*Institute of Particle Physics and Key Laboratory of Quark and Lepton Physics (MOE), Central China Normal University, Wuhan, Hubei 430079, China*

[2]*School of Physics and Electronic Information, Shangrao Normal University, Shangrao 334001, China*

[3]*Center for High Energy Physics, Peking University, Beijing 100871, China*

[4]*Institute of Particle and Nuclear Physics, Henan Normal University, Xinxiang, Henan 453007, China*

(Received 23 July 2023; revised 30 August 2023; accepted 31 October 2023; published 21 November 2023)

The absence of semitauonic decays of charmed hadrons makes the decay processes mediated by the quark-level $c \to d\tau^+\nu_\tau$ transition inadequate for probing a generic new physics (NP) with all kinds of Dirac structures. To fill in this gap, we consider in this paper the quasielastic neutrino scattering process $\nu_\tau + n \to \tau^- + \Lambda_c$, and propose searching for NP through the polarizations of the τ lepton and the Λ_c baryon. In the framework of a general low-energy effective Lagrangian, we perform a comprehensive analysis of the (differential) cross sections and polarization vectors of the process both within the Standard Model and in various NP scenarios, and scrutinize possible NP signals. We also explore the influence on our findings due to the uncertainties and the different parametrizations of the $\Lambda_c \to N$ transition form factors, and show that they have become one of the major challenges to further constrain possible NP through the quasielastic scattering process.

DOI: 10.1103/PhysRevD.108.095036

I. INTRODUCTION

Over the past few years, several intriguing anomalies have been observed in the processes mediated by the quark-level $b \to c l \bar{\nu}_l$ transitions, particularly in the ratios $R_{D^{(*)}}$ [1–11],

$$R_{D^{(*)}} \equiv \frac{\mathcal{B}(B \to D^{(*)}\tau^-\nu_\tau)}{\mathcal{B}(B \to D^{(*)}\ell^-\nu_\ell)}, \tag{1}$$

with $\ell = e, \mu$. These anomalies continuously challenge the lepton flavor universality, a central feature of the Standard Model (SM) of particle physics, and arouse a surge of phenomenological studies of new physics (NP) beyond the SM in B physics (for recent reviews, see, e.g., Refs. [12–15]). In view of the potential violation of the lepton flavor universality in B-meson decays, it is also natural to investigate if such phenomena also emerge in the charm sector.

Among the various processes used to probe the phenomena, the ones mediated by the quark-level $c \to d\tau^+\nu_\tau$ transition attract certain attention [16–19]. In particular, a ratio $R_{\tau/\mu}$, somewhat similar to $R_{D^{(*)}}$, can be defined as

$$R_{\tau/\mu} = \frac{\Gamma(D^+ \to \tau^+\nu_\tau)}{\Gamma(D^+ \to \mu^+\nu_\mu)}, \tag{2}$$

and serve as an important avenue to test the SM in the charm sector [16,17]. Interestingly enough, the ratio $R_{\tau/\mu}$ is constructed from the purely leptonic D-meson decays rather than from the semileptonic ones, which is in contrast to the ratios $R_{D^{(*)}}$. The underlying reason for this is that the largest accessible phase space for semileptonic D-meson decays is given by $m_{D^+} - m_{\pi^0} \simeq 1.735$ GeV, which is smaller than the τ-lepton mass, rendering the semitauonic D-meson decays kinematically forbidden. The same conclusion also holds for the charmed-baryon decays.

The absence of semitauonic decays of charmed hadrons makes, therefore, the decay processes mediated by the $c \to d\tau^+\nu_\tau$ transition suitable for probing NP with only a subset of Dirac structures. For example, the purely leptonic D-meson decays are known to be only sensitive to the axial and pseudoscalar four-fermion operators of a general low-energy effective Lagrangian [denoted by $\mathcal{L}_{\rm eff}$ as introduced in Eq. (3)], making the tauonic vector, scalar, and tensor operators seemingly inaccessible at the low-energy regime [18–21]. Although these operators can be probed through the high-p_T dilepton invariant mass tails at

*yarukong@mails.ccnu.edu.cn
†lailifen@mails.ccnu.edu.cn
‡xqli@mail.ccnu.edu.cn
§Corresponding author: yanxinshuai@htu.edu.cn
‖yangyd@mail.ccnu.edu.cn
¶zhengdh@mails.ccnu.edu.cn

high-energy colliders under additional assumptions [22,23], other new processes and observables, particularly the low-energy ones, are still badly needed in order to pinpoint all the possible NP Dirac structures. In some cases, these low-energy processes and observables can also provide very complementary information about NP [24,25].

In this paper, we will consider the quasielastic (QE) neutrino scattering process $\nu_\tau + n \to \tau^- + \Lambda_c$ induced by the quark-level $\nu_\tau d \to \tau^- c$ transition. This process is free from the kinematic problem that the semitauonic charmed-baryon decays face and involves all the effective operators of $\mathcal{L}_{\rm eff}$. However, even with the purely tauonic D-meson decays and the high-p_T dilepton invariant mass analyses, it still cannot provide enough observables to fully pinpoint all the NP Dirac structures and determine the corresponding complex Wilson coefficients (WCs). Thus, we will also propose searching for NP through the polarizations of the τ lepton and the Λ_c baryon.[1] The polarization observables to be considered in this work involve all the effective operators of $\mathcal{L}_{\rm eff}$, and can fill the gap (at least partially), though they are generally more difficult to measure than the cross sections. Based on a combined constraint on the WCs of the effective operators set by the measured branching ratio of $D^+ \to \tau^+ \nu_\tau$ decay [17] and the analysis of the high-p_T dilepton invariant mass tails [22], we will perform a comprehensive analysis of all the observables involved both within the SM and in various NP scenarios, and scrutinize possible NP signals.

The hadronic matrix elements of the scattering process will be parametrized by the $n \to \Lambda_c$ transition form factors, which are in turn related to the $\Lambda_c \to N$ (nucleon) form factors by complex conjugation. However, since a scattering process generally occupies a negative kinematic range ($q^2 < 0$) while a decay process happens at the positive one ($q^2 > 0$), an extrapolation of the $\Lambda_c \to N$ transition form factors from positive to negative q^2 becomes necessary. This requires that the form-factor parametrization must possess analyticity in the proper q^2 range [24,25,29]. In this paper, we will consider three different models with three different form-factor parametrizations for the $\Lambda_c \to N$ transition form factors to compute the cross sections and polarization vectors in various NP scenarios. Our major results will be, however, based on the lattice QCD (LQCD) calculations [30], since they also provide the theoretical uncertainties, which we will propagate to all the observables considered. Nonetheless, a detailed comparison of all the observables calculated with different form-factor parametrizations will be provided as well.

The paper is organized as follows. In Sec. II, we begin with a brief introduction of our theoretical framework, including the most general low-energy effective Lagrangian as well as the kinematics, the cross sections, and the various polarization vectors of the scattering process. In such a framework, we study in Sec. III A the total cross section and the averaged polarization vectors in various NP scenarios, and then in Sec. III B the differential cross sections and the Q^2-dependent polarization observables. In Sec. III C, we revisit the scattering process together with the Q^2-dependent observables in the limit of small WCs (i.e., small g_i). The subsequent two subsections contain our exploration of the influence on our findings due to the uncertainties and the different parametrizations of the $\Lambda_c \to N$ transition form factors. Finally, we collect our main conclusions in Sec. IV, and relegate further details on the form factors and explicit expressions of the various observables to the Appendixes.

II. THEORETICAL FRAMEWORK

A. Low-energy effective Lagrangian

Without introducing the right-handed neutrinos, the most general low-energy effective Lagrangian responsible for the $\nu_\tau d \to \tau^- c$ transition can be written as

$$\mathcal{L}_{\rm eff} = -\frac{4G_F}{\sqrt{2}} V_{cd} \Big[(1 + g_V^L)\mathcal{O}_V^L + g_V^R \mathcal{O}_V^R + g_S^L \mathcal{O}_S^L + g_S^R \mathcal{O}_S^R + g_T^L \mathcal{O}_T^L \Big] + \text{H.c.}, \tag{3}$$

with

$$\begin{aligned} \mathcal{O}_V^{L,R} &= (\bar{c}\gamma^\mu P_{L,R} d)(\bar{\tau}\gamma_\mu P_L \nu_\tau), \\ \mathcal{O}_S^{L,R} &= (\bar{c} P_{L,R} d)(\bar{\tau} P_L \nu_\tau), \\ \mathcal{O}_T^{L} &= (\bar{c}\sigma^{\mu\nu} P_L d)(\bar{\tau}\sigma_{\mu\nu} P_L \nu_\tau), \end{aligned} \tag{4}$$

where $P_{R,L} = (1 \pm \gamma_5)/2$ are the right- and left-handed projectors, and $\sigma^{\mu\nu} = i[\gamma^\mu, \gamma^\nu]/2$ the antisymmetric tensor. Note that the tensor operators with mixed quark and lepton chiralities vanish due to Lorentz invariance. The WCs g_i in Eq. (3) parametrize possible deviations from the SM and are complex in general. Such a framework is only applicable up to an energy scale of $\mathcal{O}(m_b)$, with m_b denoting the bottom-quark mass, above which new degrees of freedom would appear.

It should be pointed out that the $\mathcal{L}_{\rm eff}$ can also be presented in another operator basis, in which the majority of basis operators possess definite parity (see, e.g., Ref. [19]). The WCs associated with this set of basis operators can be related to the g_i in Eq. (3) through the following relations:

$$g_{V,A} = g_V^R \pm g_V^L, \qquad g_{S,P} = g_S^R \pm g_S^L, \qquad g_T = g_T^L. \tag{5}$$

And the former become very handy for discussing the D-meson leptonic decays, since these decays are only sensitive

[1] We note that the polarizations of the final lepton and the produced nucleon in a charged-current QE neutrino-nucleus scattering process induced by the quark-level $\nu_\ell d \to \ell^- u$ or $\bar{\nu}_\ell u \to \ell^+ d/s$ transition have also been discussed in Refs. [26–28].

to g_A and g_P, as shown in Eq. (23). However, we will focus on the operators listed in Eq. (4), since we will also take account of the constraints set through the analysis of the dilepton invariant mass tails in $pp \to \tau\nu_\tau$ processes at high p_T [22], which are based on the very same set of basis operators as in Eq. (4) and much severer in general than the ones set by the $D^+ \to \tau^+\nu_\tau$ decay (see the colored regions in Fig. 2).

B. Cross section, form factors, and kinematics

The differential cross section of the QE scattering process $\nu_\tau(k)+n(p)\to\tau^-(k')+\Lambda_c(p')$, with $p=(m_n,0)$, $p'=(E_{\Lambda_c},\boldsymbol{p}')$, $k=(E,\boldsymbol{k})$, and $k'=(E',\boldsymbol{k}')$, is given by

$$d\sigma = \frac{1}{4p\cdot k}\frac{d^3\boldsymbol{k}'}{(2\pi)^3}\frac{1}{2E'}\frac{d^3\boldsymbol{p}'}{(2\pi)^3}\frac{1}{2E_{\Lambda_c}}\overline{|\mathcal{M}|^2} \times (2\pi)^4\delta^4(p+k-p'-k'), \tag{6}$$

where the amplitude $\mathcal{M}$ can be generically written as [31]

$$\mathcal{M} = \frac{4G_F}{\sqrt{2}}V_{cd}\left(J_H J^L + J_H^\alpha J_\alpha^L + J_H^{\alpha\beta}J_{\alpha\beta}^L\right), \tag{7}$$

when all the effective operators in Eq. (3) are taken into account. The lepton currents in Eq. (7) are defined as

$$J^L_{(\alpha\beta)} = \bar{u}_\tau(k',r')\Gamma_{(\alpha\beta)}P_L u_{\nu_\tau}(k,r), \tag{8}$$

with $\Gamma_{(\alpha\beta)}=(1,\gamma_\alpha,\sigma_{\alpha\beta})$, while the hadron currents as

$$J_H^{(\alpha\beta)} = \langle\Lambda_c(p',s')|\bar{c}O_H^{(\alpha\beta)}d|n(p,s)\rangle, \tag{9}$$

with

$$O_H = \frac{1}{2}(g_S+g_P\gamma_5),$$
$$O_H^\alpha = \frac{1}{2}\gamma^\alpha(g'_V-g'_A\gamma_5),$$
$$O_H^{\alpha\beta} = g_T^L\sigma^{\alpha\beta}P_L, \tag{10}$$

where $g'_{V,A}=(1+g_V^L\pm g_V^R)$, $g_{S,P}$ are given by Eq. (5), and r and s (r' and s') denote the spins of initial (final) lepton and baryon, respectively. The amplitude squared $|\mathcal{M}|^2$ is obtained by summing up the initial- and final-state spins; more details are elaborated in Appendix B.

The hadronic matrix elements $\langle\Lambda_c|\bar{c}O_H^{(\alpha\beta)}d|n\rangle$ in Eq. (9) are identical to the complex conjugate of $\langle n|(\bar{c}O_H^{(\alpha\beta)}d)^\dagger|\Lambda_c\rangle$, which are further parametrized by the $\Lambda_c\to N$ transition form factors [30,32,33]. Since a scattering process generally occupies a different kinematic range ($q^2<0$) from that of a decay ($q^2>0$), theoretical analyses of the scattering process require an extrapolation of the form factors to negative q^2. Thus, the form-factor parametrizations suitable for our purpose must be analytic in the proper q^2 range.

Interestingly, there exist already several schemes that meet our selection criterion and have been utilized to parametrize the $\Lambda_c\to N$ form factors by various models. For instance, a dipole parametrization scheme has been employed within the MIT bag model (MBM) [34,35] and the nonrelativistic quark model (NRQM) [36], and a double-pole one in the relativistic constituent quark model (RCQM) [37,38]. Although the form-factor parametrizations in each scheme do not result in pathological behaviors in the $q^2<0$ range, only the form factors associated with the matrix element $\langle N|\bar{d}\gamma^\mu P_L c|\Lambda_c\rangle$ were calculated in these models. The primary scheme we consider was initially proposed to parametrize the $B\to\pi$ vector form factor [39], and has been recently utilized in the LQCD calculations of the $\Lambda_c\to N$ transition form factors [30]. In contrast to other model evaluations, the LQCD calculation not only takes care of all the form factors, but also provides an error estimation. Thus, we will adopt the latest LQCD results [30] throughout this work. Meanwhile, given that the model calculations of the $N\to\Lambda_c$ form factors can significantly affect the predictions of Λ_c weak production in neutrino QE processes [29,40], we will also analyze the QE scattering process $\nu_\tau+n\to\tau^-+\Lambda_c$ in terms of the form factors calculated within the models MBM, NRQM, and RCQM in various NP scenarios; for more details about the form factors in these different models, we refer the readers to Appendix A.

The kinematics of the QE scattering process is bounded by [24]

$$\frac{\alpha-E\sqrt{\lambda}}{m_n+2E}\le q^2\le\frac{\alpha+E\sqrt{\lambda}}{m_n+2E}, \tag{11}$$

where

$$\alpha \equiv E(m_{\Lambda_c}^2-m_n^2+m_\tau^2-2m_nE)+m_nm_\tau^2,$$
$$\lambda \equiv m_{\Lambda_c}^4+(m_n^2+2m_nE-m_\tau^2)^2 - 2m_{\Lambda_c}^2(m_n^2+2m_nE+m_\tau^2).$$

This condition indicates that the neutrino beam energy E determines the maximal and minimal values of Q^2 ($Q^2=-q^2$), which, in turn, implies that any constraints on $Q^2_{\rm max}$ and $Q^2_{\rm min}$ restrict the E selection. An explicit example is that a minimal requirement for E ($E\gtrsim 8.33$ GeV) of the scattering process can be obtained by using the condition $Q^2_{\rm max}=Q^2_{\rm min}$; this can also be visualized in Fig. 1 by noting the intersection point of the red and green curves that represent the E-$Q^2_{\rm max}$ and E-$Q^2_{\rm min}$ relations, respectively. Besides the kinematic constraint on $Q^2_{\rm max}$, we also consider the limit from our theoretical framework. As our analyses are carried out in the framework of $\mathcal{L}_{\rm eff}$ given by Eq. (3), to ensure the validity of our results, we require $Q^2_{\rm max}$ to not exceed

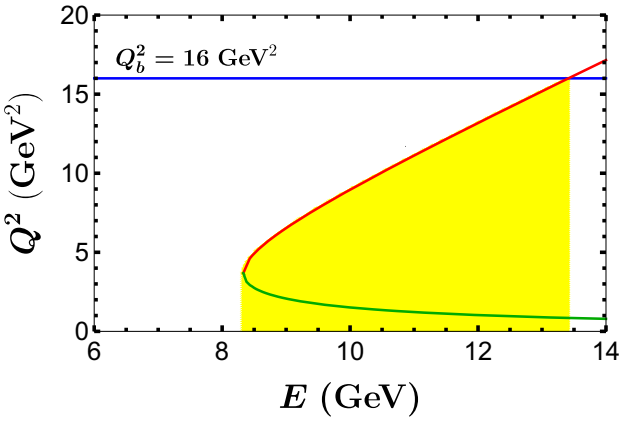

FIG. 1. Criteria for selecting the neutrino beam energy E, where the red (green) curve denotes the E-$Q^2_{\mathrm{max(min)}}$ relation given by Eq. (11), and the blue line represents the condition $Q^2 \leq 16\ \mathrm{GeV}^2$ required by our theoretical framework. The yellow range indicates the eligible E.

$Q_b^2 = 16\ \mathrm{GeV}^2 \approx m_b^2$. Such a requirement, depicted by the blue line in Fig. 1, indicates an upper bound $E \lesssim 13.41$ GeV, provided that the observables one is interested in, such as the total cross section, involve Q^2_{max}. Otherwise, E is not bounded from above, since one can always concentrate on the lower Q^2 range, even though a high Q^2_{max} is available due to a high E.

It is interesting to note that the τ-optimized ν_τ flux at the Deep Underground Neutrino Experiment (DUNE) drops below $10^8\ \mathrm{m}^{-2}\,\mathrm{year}^{-1}$ at $E_{\nu_\tau} \gtrsim 14$ GeV [41,42], which is close to the upper bound of E shown in Fig. 1. If the proposed QE scattering process were measured at the DUNE, one could then explore all the observables considered in this work within the whole, available Q^2 range, while maintaining a relatively high ν_τ beam flux. It should be pointed out that the neutrino oscillation experiments in the few-GeV range at DUNE use detectors constructed of liquid argon (see, e.g., Ref. [43]), where nuclear effects are significant. But the knowledge of those effects remains imperfect, which induces important uncertainties for the experiments of neutrino oscillation as well as the proposed QE scattering process at DUNE.

C. Polarization vectors of the final lepton and baryon

The polarization four-vector $\mathcal{P}_l^\mu$ of the τ lepton produced in the scattering process $\nu_\tau + n \to \tau^- + \Lambda_c$ can be conveniently obtained by using the density matrix formalism as [44]

$$\mathcal{P}_l^\mu = \frac{\mathrm{Tr}[\rho_l(k')\gamma^\mu\gamma_5]}{\mathrm{Tr}[\rho_l(k')]}, \tag{12}$$

where the spin density matrix $\rho_l(k')$ of the τ lepton is given by

$$\rho_l(k') = \mathcal{J}^{(\alpha\beta,\alpha'\beta')}\Big[\Lambda(k')\Gamma_{(\alpha\beta)}P_L\Lambda(k)P_R\tilde{\Gamma}_{(\alpha'\beta')}\Lambda(k')\Big]. \tag{13}$$

Now a clarification of the various symbols in Eq. (13) is in order. First, the hadronic tensor $\mathcal{J}^{(\alpha\beta,\alpha'\beta')}$ is given by

$$\begin{aligned}\mathcal{J}^{(\alpha\beta,\alpha'\beta')} &= \frac{1}{2}\sum_{ss'} J_H^{(\alpha\beta)} J_H^{(\alpha'\beta')\dagger} \\ &= \frac{1}{2}\mathrm{Tr}\Big[\Lambda(p')\mathcal{M}^{(\alpha\beta)}\Lambda(p)\widetilde{\mathcal{M}}^{(\alpha'\beta')}\Big],\end{aligned} \tag{14}$$

where $\mathcal{M}_{(\alpha\beta)}$ denotes the Dirac γ structure of the hadronic matrix element $\langle\Lambda_c|\bar{c}O_H^{(\alpha\beta)}d|n\rangle$ in Eq. (9). Clearly, $\mathcal{M}_{(\alpha\beta)}$ involves not only the WCs g_i but also the form factors. The prefactor $1/2$ accounts for the spin average over the neutron spin. Second, $\widetilde{\mathcal{M}}^{(\alpha'\beta')} = \gamma^0\mathcal{M}^{(\alpha'\beta')\dagger}\gamma^0$, $\tilde{\Gamma}_{(\alpha'\beta')} = \gamma^0\Gamma^\dagger_{(\alpha'\beta')}\gamma^0$, and $\Lambda(k) = (\not{k} + m_k)$ is the spin projection operator for a spin $1/2$ fermion with momentum k and mass m_k.

The polarization four-vector $\mathcal{P}_h^\mu$ of the produced Λ_c baryon can be obtained in a similar way, with the spin density matrix $\rho_h(p')$ given by

$$\rho_h(p') = \mathcal{L}_{(\alpha\beta,\alpha'\beta')}\Big[\Lambda(p')\mathcal{M}^{(\alpha\beta)}\Lambda(p)\widetilde{\mathcal{M}}^{(\alpha'\beta')}\Lambda(p')\Big], \tag{15}$$

where the leptonic tensor $\mathcal{L}_{(\alpha\beta,\alpha'\beta')}$ can be written as

$$\begin{aligned}\mathcal{L}_{(\alpha\beta,\alpha'\beta')} &= \frac{1}{2}\sum_{rr'} J^L_{(\alpha\beta)} J^{L\dagger}_{(\alpha'\beta')} \\ &= \frac{1}{2}\mathrm{Tr}\Big[\Lambda(k')\Gamma_{(\alpha\beta)}P_L\Lambda(k)P_R\tilde{\Gamma}_{(\alpha'\beta')}\Big].\end{aligned} \tag{16}$$

The polarization vectors $\mathcal{P}^\mu_{l,h}$ of the outgoing lepton and baryon can be decomposed as

$$\mathcal{P}^\mu_{l,h} = P_L^{l,h}(N_L^{l,h})^\mu + P_P^{l,h}(N_P^{l,h})^\mu + P_T^{l,h}(N_T^{l,h})^\mu, \tag{17}$$

where the two sets of four-vectors $N_L^{l,h}$, $N_T^{l,h}$, and $N_P^{l,h}$ are defined, respectively, as

$$\begin{aligned}(N_L^l)^\mu &= \left(\frac{|\boldsymbol{k}'|}{m_\tau}, \frac{k'^0\boldsymbol{k}'}{m_\tau|\boldsymbol{k}'|}\right), \\ (N_T^l)^\mu &= \left(0, \frac{\boldsymbol{k}\times\boldsymbol{k}'}{|\boldsymbol{k}\times\boldsymbol{k}'|}\right), \\ (N_P^l)^\mu &= \left(0, \frac{\boldsymbol{k}'\times(\boldsymbol{k}\times\boldsymbol{k}')}{|\boldsymbol{k}'\times(\boldsymbol{k}\times\boldsymbol{k}')|}\right),\end{aligned} \tag{18}$$

and

TABLE I. Values of the input parameters relevant for Eq. (23), which are all from Ref. [47].

Parameter	Value
m_τ	1.77686 GeV
m_{D^+}	1.86965 GeV
τ_{D^+}	1.04 ps
G_F	1.1663787×10^{-5} GeV^{-2}
m_c	1.27 GeV
m_d	0 MeV

$$(N_L^h)^\mu = \left(\frac{|\boldsymbol{p}'|}{m_{\Lambda_c}}, \frac{p'^0 \boldsymbol{p}'}{m_{\Lambda_c}|\boldsymbol{p}'|}\right),$$
$$(N_T^h)^\mu = \left(0, \frac{\boldsymbol{p}' \times \boldsymbol{k}}{|\boldsymbol{p}' \times \boldsymbol{k}|}\right),$$
$$(N_P^h)^\mu = \left(0, \frac{\boldsymbol{p}' \times (\boldsymbol{p}' \times \boldsymbol{k})}{|\boldsymbol{p}' \times (\boldsymbol{p}' \times \boldsymbol{k})|}\right), \tag{19}$$

indicating the longitudinal (L), transverse (T), and perpendicular (P) directions of the final τ lepton and Λ_c baryon in their reaction planes accordingly. It is then fairly straightforward to obtain the components of $\mathcal{P}^\mu$ in Eq. (17) through

$$P_a^{l,h} = -(\mathcal{P} \cdot N_a^{l,h}), \qquad a = L, P, T. \tag{20}$$

In order to study the dependence of these polarization vectors on the neutrino energy E, one often introduces the average polarizations $\langle P_a^{l,h} \rangle$, which are defined as [26,45]

$$\langle P_a^{l,h} \rangle = \frac{\int_{Q^2_{\min}}^{Q^2_{\max}} P_a^{l,h}(Q^2) \frac{d\sigma}{dQ^2} dQ^2}{\int_{Q^2_{\min}}^{Q^2_{\max}} \frac{d\sigma}{dQ^2} dQ^2}. \tag{21}$$

To characterize the overall degree of polarization of the outgoing particles, one can also define the overall average polarization $\langle P^{l,h} \rangle$ as

$$\langle P^{l,h} \rangle = \sqrt{\langle P_L^{l,h} \rangle^2 + \langle P_P^{l,h} \rangle^2 + \langle P_T^{l,h} \rangle^2}. \tag{22}$$

D. Constraints on the WCs of $\mathcal{L}_{\text{eff}}$

Here we discuss briefly the most relevant and stringent constraints on the WCs g_i from the charmed-hadron weak decays and the high-p_T dilepton invariant mass tails.

Given that the semitauonic decays of charmed hadrons are kinematically forbidden, the D-meson tauonic decays become the only decay processes that can be used to constrain the WCs g_i in Eq. (3). Here we consider the $D^+ \to \tau^+ \nu_\tau$ decay with its branching ratio given by [18,19,46]

$$\mathcal{B}(D^+ \to \tau^+ \nu_\tau) = \frac{G_F^2 |V_{cd}|^2 f_{D^+}^2 m_{D^+} m_\tau^2}{8\pi} \left(1 - \frac{m_\tau^2}{m_{D^+}^2}\right)^2 \times \left|1 - g_A + g_P \frac{m_{D^+}^2}{m_\tau (m_c + m_d)}\right|^2 \tau_{D^+}, \tag{23}$$

where g_A and g_P are introduced in Eq. (5). With the inputs listed in Table I, $|V_{cd}| = 0.22438 \pm 0.00044$ from the global fit [47], and $f_{D^+} = 212.0 \pm 0.7$ MeV from an average of the LQCD simulations [48–50], we can obtain the parameter space of the WCs g_i allowed by the measured branching fraction $\mathcal{B}(D^+ \to \tau^+ \nu_\tau) = (1.20 \pm 0.24_{\text{stat}} \pm 0.12_{\text{syst}}) \times 10^{-3}$ [17]; similar works have also been conducted in Refs. [18,19]. At the same time, constraints on these WCs can also be set through the analysis of the dilepton invariant mass tails in $pp \to \tau\nu_\tau$ processes at high p_T [22].

We combine in Fig. 2 the aforementioned constraints at the 1σ level. It can be seen that the most stringent constraints on g_S^L, g_S^R, and g_T^L are set by the high-p_T dilepton invariant mass tails, whereas the bound on g_V^R is entirely dominated by the measured branching fraction of $D^+ \to \tau^+ \nu_\tau$ decay. Meanwhile, although the boundary of the real part of g_V^L is set by the high-p_T dilepton invariant mass tails, the imaginary part is bounded by the $D^+ \to \tau^+ \nu_\tau$ decay, as indicated by the overlapped region in color. It should be pointed out that all the constraints denoted by the colored regions in Fig. 2 are obtained by setting the rest of WCs to zero. In order to fully constrain the NP operators in Eq. (3), more processes and observables are clearly needed.

Our proposed QE scattering process together with the polarization vectors, as will be shown in the next section, is

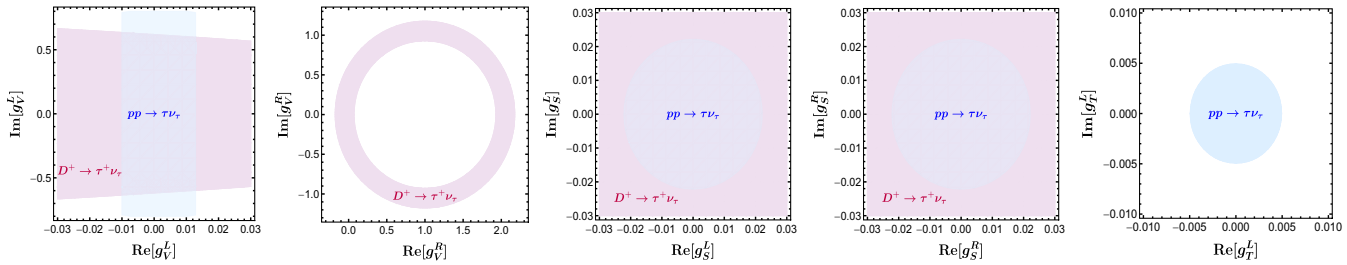

FIG. 2. Constraints on the WCs g_i within the 1σ level. The region colored in pink is set by the measured branching fraction of $D^+ \to \tau^+ \nu_\tau$ decay [17], while the region colored in light blue is allowed by the high-p_T dilepton invariant mass tails in $pp \to \tau\nu_\tau$ processes [22].

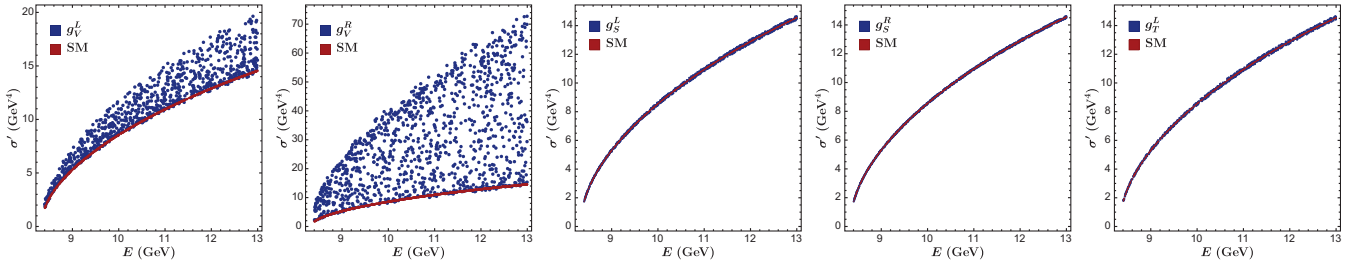

FIG. 3. The total cross section σ', with $\sigma' = 8\pi m_n^2\sigma/(G_F^2|V_{cd}|^2)$, of the scattering process $\nu_\tau + n \to \tau^- + \Lambda_c$ as a function of the neutrino energy E. The dark red curve denotes the SM contribution, while the dark blue points represent the total contributions from both the SM and the NP in the presence of a single g_i, whose values are varied randomly within the overlapped regions in color shown in Fig. 2.

exactly what one is looking for. Before delving into detailed numerical analyses to justify this statement, let us take the g_V^R case (i.e., except for $g_V^R \neq 0$ all the other WCs vanish) for a simple illustration. From Fig. 2 we have observed that the WC g_V^R is solely constrained by the $D^+ \to \tau^+\nu_\tau$ decay, as denoted by the pink ring area. For simplicity, let us drop the errors of the constraint for the moment, so that the ring now becomes a circle [see Eq. (23)]. Meanwhile, the (differential) cross section of our proposed scattering process can also provide a constraint, which will be denoted by another circle [see Eq. (B1)]. Assuming these two circles intersect at two points—as it happens quite often—one then obtains two sets of possible values for the real and imaginary parts of g_V^R. To further identify the correct one, one must invoke another observable that involves g_V^R. Clearly, the detailed formulas of $P_a^{l,h}$ in Appendix C indicate that those polarization observables can fill the gap. Nevertheless, it should be pointed out that compared with the cross sections of the scattering process, the polarization observables are generally more difficult to measure, and thus it will be experimentally more demanding to obtain the same accuracy of those observables as of the cross sections.

III. NUMERICAL RESULTS AND DISCUSSIONS

A. Total cross section and average polarizations

We start with studying the dependence of the total cross section σ', with $\sigma' = 8\pi m_n^2\sigma/(G_F^2|V_{cd}|^2)$, and the average polarizations $\langle P_a^{l,h}\rangle$ on the neutrino energy E. To this end, by considering the range $E \in [8.33, 13]$ GeV and varying randomly the WCs g_i within the overlapped regions in color shown in Fig. 2, we plot in Fig. 3 the total cross section σ of the scattering process $\nu_\tau + n \to \tau^- + \Lambda_c$ as a function of E, both within the SM and in various NP scenarios.[2] It can be seen that a few interesting features already emerge. First, a higher beam energy clearly favors a larger total cross section. Second, the cross section can be significantly affected by the allowed parameter space of g_V^R and g_V^L shown in Fig. 3, especially by the former. This in turn indicates a larger opportunity for improving the limits on $g_V^{L,R}$ through the proposed QE scattering process. On the other hand, for g_S^L, g_S^R, and g_S^T, stringent constraints from the high-p_T dilepton invariant mass tails do not leave much room for possible deviations from the SM predication. Thus, to further improve the constraints on these g_i, demanding experimental setup for the scattering process is certainly necessary. Finally, although the allowed parameter spaces for g_S^L and g_S^R are identical to each other [see Eq. (23) and Fig. 2], their imprints on the total cross section are slightly different, especially at the high-E range, as shown vaguely in Fig. 3. Such a small difference in fact results from the different interference between $\mathcal{O}_V^L$ and $\mathcal{O}_S^{L,R}$; more details could be found in Appendix B.

In Fig. 4, we show the average polarizations $\langle P_L^l\rangle$, $\langle P_P^l\rangle$, $\langle P_T^l\rangle$, and $\langle P^l\rangle$ of the τ lepton as a function of the neutrino beam energy E in various scenarios. Let us start with the SM case. As depicted by the red curves in Fig. 4, both the absolute values of $\langle P_L^l\rangle$ and $\langle P^l\rangle$ increase along with the increase of E, which is not surprising, since the τ lepton produced through the scattering process $\nu_\tau + n \to \tau^- + \Lambda_c$ is left-handed in the SM. On the other hand, $\langle P_P^l\rangle$ reaches its peak around $E = 10$ GeV, while $\langle P_T^l\rangle = 0$ irrespective of E because P^l in this case misses the terms containing $\varepsilon_{\{k\}\{k'\}\{N_a\}\{p\}}$,[3] which essentially characterize the T component of P^l; see Appendix C for more details. Note that $\langle P_T^l\rangle = 0$ in the SM qualifies itself as a null test observable. Measuring a tiny but nonzero $\langle P_T^l\rangle$ induced by NP effects could be, however, challenging, as indicated by the plots in the third column of Fig. 4.

We now move on to the NP scenarios. From the four figures on the top panel in Fig. 4, we observe that

[2]For simplicity, we will neglect the possible nuclear effects [26,51–54] when discussing all the observables, which induce additional important uncertainties besides the experimental ones and the ones to be discussed in the Secs. III D and III E.

[3]Note that $P_T^{l,h}$ will also vanish if all the WCs g_i are real, since $\varepsilon_{\{k\}\{k'\}\{N_a\}\{p\}}$ is always accompanied by the imaginary unit i, as shown in Appendix C.

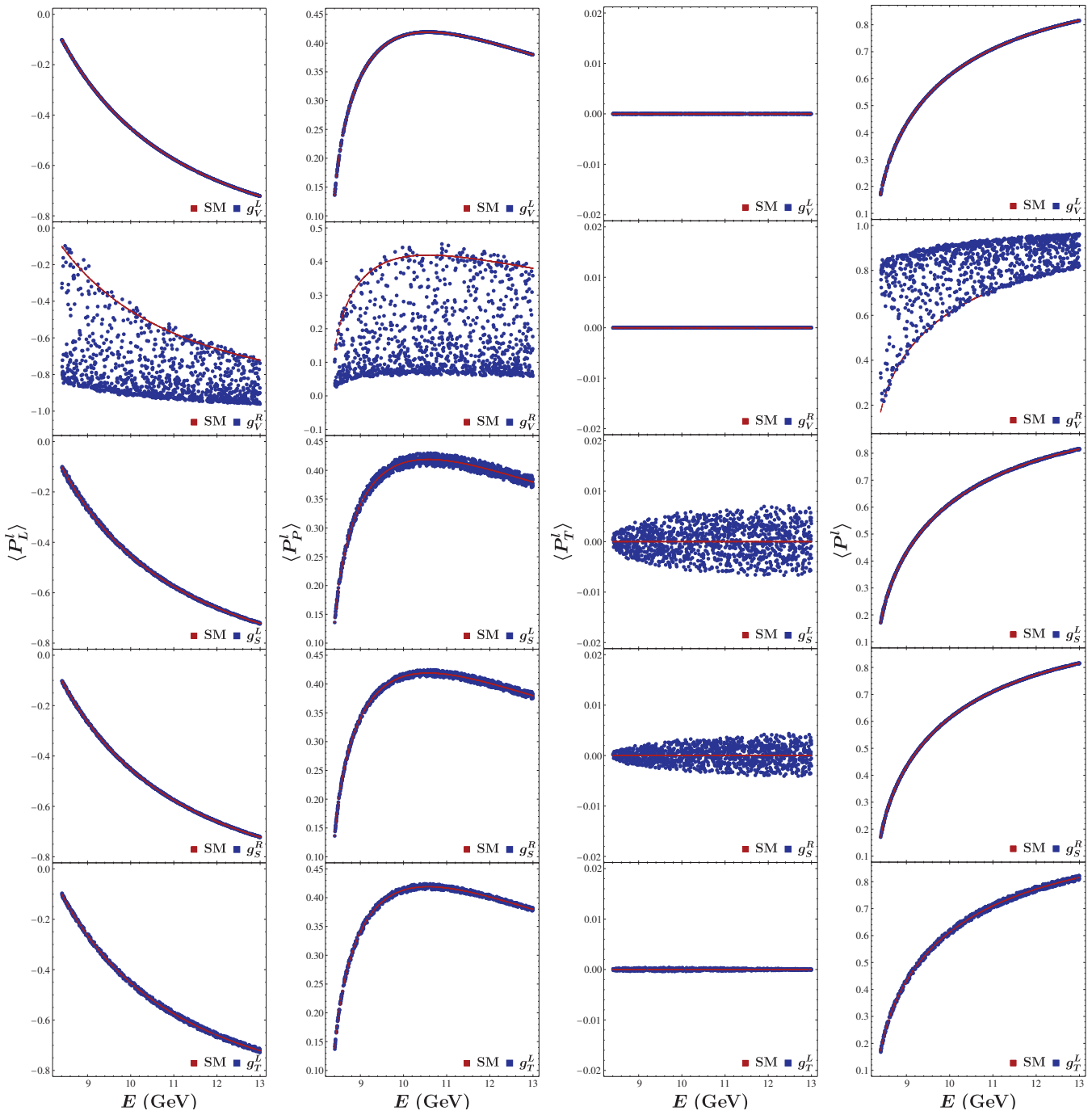

FIG. 4. The average polarizations $\langle P_L^l \rangle$, $\langle P_P^l \rangle$, $\langle P_T^l \rangle$, and $\langle P^l \rangle$ for the scattering process $\nu_\tau + n \to \tau^- + \Lambda_c$ as a function of the neutrino energy E. The color captions are the same as in Fig. 3.

contributions to the average polarization $\langle P_a^l \rangle$ from the SM and the WC g_V^L are indistinguishable, because they share the same effective operator $\mathcal{O}_V^L$ [see Eq. (3)]. For the WC g_V^R, on the other hand, large deviations of $\langle P_{L,P}^l \rangle$ from their SM predictions are possible due to the sizable allowed parameter space of g_V^R, while $\langle P_T^l \rangle$ still remains zero in this case due to the same reason as in the SM. Similar to the case of total cross section, possible deviations of all $\langle P_a^l \rangle$ from their SM predictions are relatively small for the WCs g_S^L, g_S^R, and g_T^L due to the stringent constraints on them from the current data, as shown in Fig. 2.

Similar to the SM case, we can make the following observations in the NP scenarios. First, there exist small differences between $\langle P_a^l \rangle$ associated with the WCs g_S^L and g_S^R due to their different operator structures. One can see that the overall blue bands from g_S^L are slightly broader than

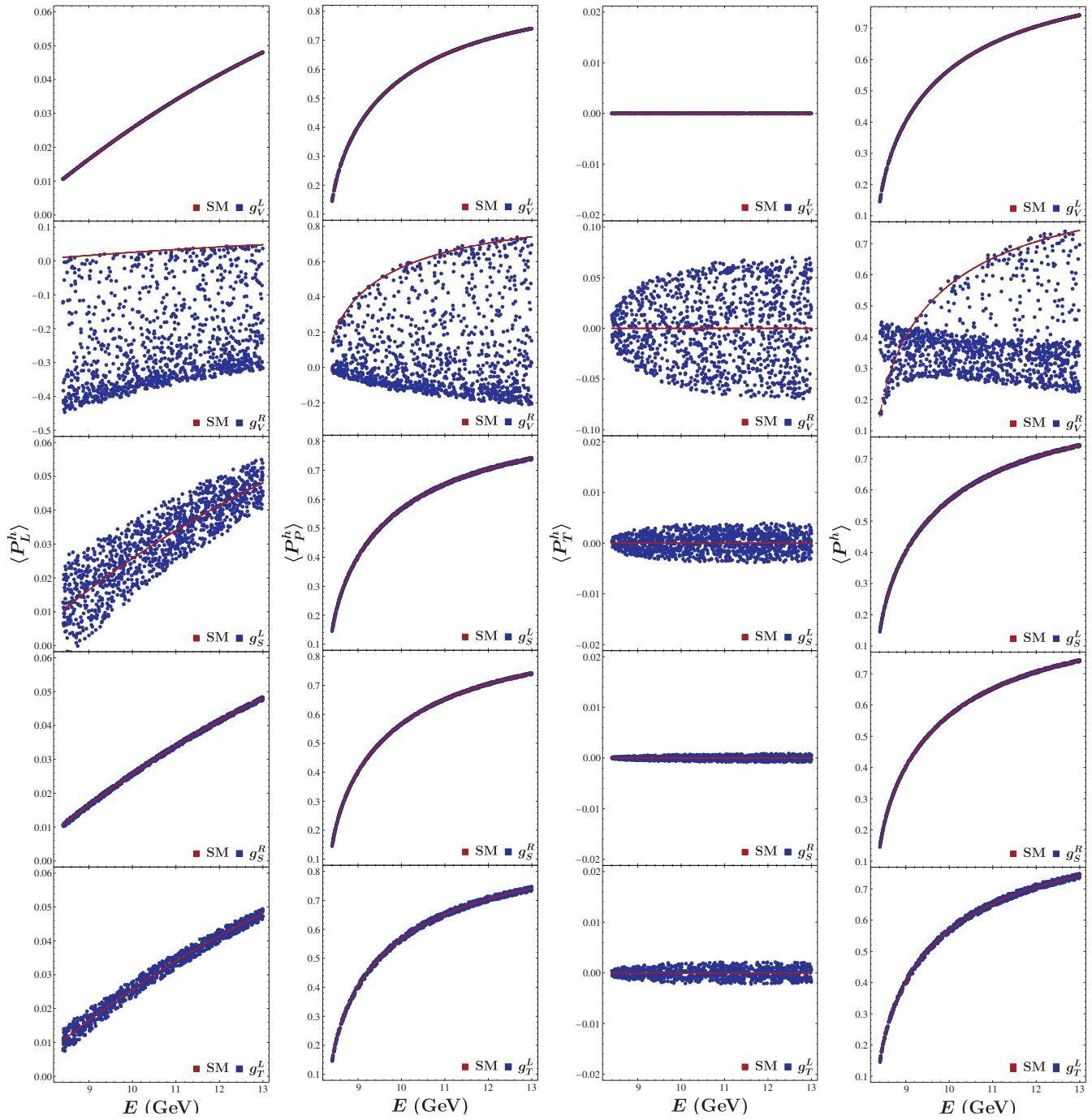

FIG. 5. The average polarizations $\langle P_L^h \rangle$, $\langle P_P^h \rangle$, $\langle P_T^h \rangle$, and $\langle P^h \rangle$ for the scattering process $\nu_\tau + n \to \tau^- + \Lambda_c$ as a function of the neutrino energy E. The color captions are the same as in Fig. 3.

from g_S^R in the $\langle P_a^l \rangle$-E planes. Second, the fuzzy blue bands in the $\langle P_L^l \rangle$-E plane from $g_S^{L,R}$ imply that a relatively low E is more favored to further constrain these two WCs, whereas a relatively high E would be more advantaged for further limiting g_T^L through $\langle P_L^l \rangle$. The situation is, however, totally opposite in probing g_S^L, g_S^R, and g_T^L through $\langle P_T^l \rangle$. Finally, only a relatively high E is favored for probing g_S^L, g_S^R, and g_T^L through $\langle P_P^l \rangle$.

We also show in Fig. 5 the average polarizations $\langle P_L^h \rangle$, $\langle P_P^h \rangle$, $\langle P_T^h \rangle$, and $\langle P^h \rangle$ of the Λ_c baryon as a function of E. Contrary to the τ-lepton case, the predominant polarization mode of the Λ_c baryon produced through the QE scattering process is perpendicular in the SM. Although $\langle P_L^h \rangle$ increases along with the increase of E, its overall polarization degree is only of $\mathcal{O}(10^{-2})$. Meanwhile, $\langle P_T^h \rangle$ is always zero irrespective of E for a similar reason as $\langle P_T^l \rangle$ in the τ-lepton case.

For the NP scenarios in this case, we observe some similar features too. First, the average polarizations $\langle P_a^h \rangle$ induced by g_V^L are also indistinguishable from the SM case, as shown by the first four plots on the top panel in Fig. 5, due to the same reason as mentioned in the τ-lepton case. Second, a large opportunity exists clearly for improving the limit on g_V^R through the measurements of these polarization vectors of the Λ_c baryon. Note that, contrary to $\langle P_T^l \rangle$, $\langle P_T^h \rangle$ would be nonzero in the presence of the very same NP scenario. Finally, all $\langle P_a^h \rangle$ induced by g_S^L, g_S^R, and g_T^L are small due to the stringent constraints on these WCs. However, given the small value of $\langle P_L^h \rangle$ predicted in the SM, possible deviations induced by these NP effects, especially by g_S^L, could still reach more than 100% at the low-E range.

B. Differential cross section and Q^2-dependent polarizations

Taking into account the interesting behavior of $\langle P_P^l \rangle$ shown in Fig. 4 and the neutrino beam flux at the DUNE [41,42], we will set $E = 10$ GeV as our benchmark beam energy and explore how the differential cross section and the polarizations $P_a^{l,h}$ vary with respect to Q^2. To this end, by letting the WCs g_i vary randomly within the overlapped regions in color shown in Fig. 2, we plot in Fig. 6 the resulting differential cross sections and polarizations P_a^l as a function of Q^2 in various NP scenarios, together with the SM predictions. Let us scrutinize the SM case first. As indicated by the red curves in Fig. 6, the differential cross section of the scattering process clearly prefers the low-Q^2 range in the SM. A similar conclusion also holds for the polarization P_L^l, even though it experiences a crossover at $Q^2 \simeq 8$ GeV^2. P_P^l peaks roughly at $Q^2 \simeq 8$ GeV^2, while unsurprisingly P_T^l remains zero irrespective of Q^2.

We now move on to discuss the NP scenarios shown in Fig. 6, from which an overall pattern similar to that found in the previous subsection is observed. First, large deviations from the SM prediction for the differential cross section are only possible for $g_V^{L,R}$, while large deviations for the polarizations $P_{L,P}^l$ can be expected only for g_V^R. Second, due to the stringent experimental constraints on g_S^L, g_S^R, and g_T^L, deviations from the SM predictions for the differential cross section and the polarizations P_a^l in these three NP scenarios become much smaller.

To have a clearer view of these deviations from the corresponding SM predictions, let us define $\delta[d\sigma']/dQ^2 = d\sigma'/dQ^2|_{\rm NP} - d\sigma'/dQ^2|_{\rm SM}$ and $\delta P_a^{l,h} = P_a^{l,h}|_{\rm NP} - P_a^{l,h}|_{\rm SM}$, and plot them explicitly in Fig. 7. It can be seen that the deviations δP_a^l remain zero for the g_V^L scenario, making the (differential) cross section the only avenue to probe g_V^L through the scattering process. For g_V^R, a relatively high Q^2 is certainly preferred to observe the potentially maximum deviations of $\delta P_{L,P}^l$ but at the expense of observing the maximum deviation of the differential cross section, whereas $\delta P_T^l = 0$ in the whole Q^2 range. In the case of g_S^L and g_S^R, the overall deviation patterns are similar for the three polarizations P_a^l, but opposite for the differential cross section. Nonetheless, a relatively high Q^2, e.g., $Q^2 \simeq 7.5$ GeV^2, can be of benefit for probing g_S^L and g_S^R through these observables. In the presence of g_T^L, on the other hand, the situation is a little complicated. From the four plots on the bottom panel, we observe that the low-Q^2 range clearly favors the deviations of the differential cross section and the polarization P_L^l, whereas the slightly high-Q^2 range favors the deviations $\delta P_{P,T}^l$. Overall, the maximum δP_L^l and δP_P^l could reach 1 and 0.45 in the g_V^R scenario, respectively. However, the maximum δP_L^l for the g_S^L, g_S^R, and g_T^L scenarios could only amount to 0.02 at most, and the situation is even more challenging for $\delta P_{P,T}^l$.

Similar analyses can be applied to the polarizations P_L^h, P_P^h, and P_T^h of the Λ_c baryon. In Fig. 8, we show the variations of these observables with respect to Q^2 both within the SM and in the various NP scenarios. It is found that P_a^h exhibit similar characteristics as P_a^l shown in Fig. 6. For instance, both P_T^l and P_T^h remain zero irrespective of the kinematics Q^2. In addition, both P_L^l and P_L^h experience a crossover and peak at the low-Q^2 range. Finally, both P_P^l and P_P^h drop down to zero at $Q^2_{\rm min}$ and $Q^2_{\rm max}$. Nevertheless, distinct differences between these two sets of observables are also observed. An obvious example is that P_P^l and P_P^h peak at different Q^2, $Q^2 \simeq 7$ GeV^2 for the former whereas $Q^2 \simeq 4$ GeV^2 for the later. In addition, the crossover positions of P_L^l and P_L^h lie at different Q^2, $Q^2 \simeq 8$ GeV^2 for the former whereas $Q^2 \simeq 4$ GeV^2 for the later.

With regard to δP_a^h, the deviations from the corresponding SM predictions for the polarizations P_a^h, our results are shown in Fig. 9. Compared to the deviations δP_a^l shown in Fig. 7, δP_a^h are characterized by some new features. First, for the g_V^R scenario, in contrast to δP_L^l and δP_P^l, δP_L^h and δP_P^h prefer a relatively low Q^2, which is also favored by the deviation of the differential cross section shown in Fig. 7. In addition, contrary to δP_T^l, δP_T^h is not equal to zero in this scenario. Second, the overall sizes of δP_a^h in the presence of g_S^L, g_S^R, and g_T^L are smaller than that of δP_a^l, especially of $\delta P_{P,T}^l$. Finally, for the g_S^R and g_T^L scenarios, the minima of δP_L^h arise both at the medium-Q^2 range, whereas the minima of δP_L^l arise at the $Q^2_{\rm min}$ and $Q^2_{\rm max}$, respectively.

Thus far, we have explored in detail the behaviors of the differential cross section and the polarizations $P_a^{l,h}$ with respect to Q^2 and pointed out the possible Q^2 regions, in which these observables reach their maxima in various scenarios. However, we have not provided any explanations of these observed behaviors. We will postpone it to the next subsection, where it will be worked out in the small-g_i limit.

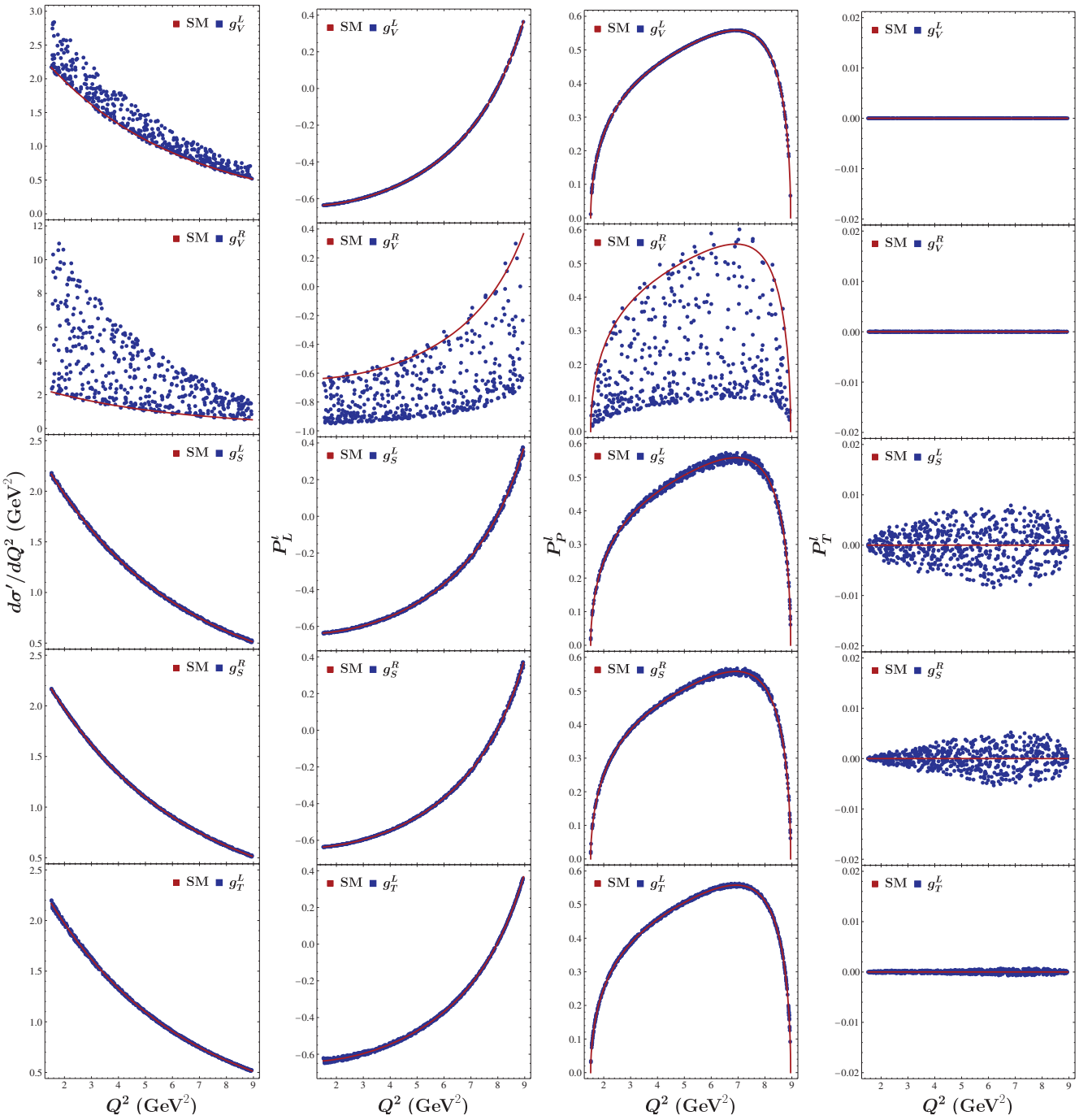

FIG. 6. Variations of the differential cross section as well as the polarizations P_L^l, P_P^l, and P_T^l with respect to Q^2, where we have set the neutrino beam energy at $E = 10$ GeV, after taking into account the interesting behavior of $\langle P_P^l \rangle$ shown in Fig. 4 and the neutrino beam flux at the DUNE [41,42]. The color captions are the same as in Fig. 3.

C. Polarization observables in the small-g_i limit

In the previous subsections, we have let the WCs g_i vary randomly within the overlapped regions in color shown in Fig. 2, which are set by the measured branching fraction of $D^+ \to \tau^+ \nu_\tau$ decay [17] and the high-p_T dilepton invariant mass tails in $pp \to \tau\nu_\tau$ processes [22]. However, the stringent experimental constraints on g_S^L, g_S^R, and g_T^L, together with the overall small deviations $\delta P_a^{l,h}$ shown in Figs. 7 and 9, strongly motivate us to focus on the small-g_i regions. In this case, we can expand the polarizations $P_a^{l,h}$ in terms of g_i and keep only the terms up to $\mathcal{O}(g_i)$. As will be shown in the following, examining $P_a^{l,h}$ in such a limit can shed light on the interesting behaviors of the deviations $\delta P_a^{l,h}$ shown in Figs. 7 and 9.

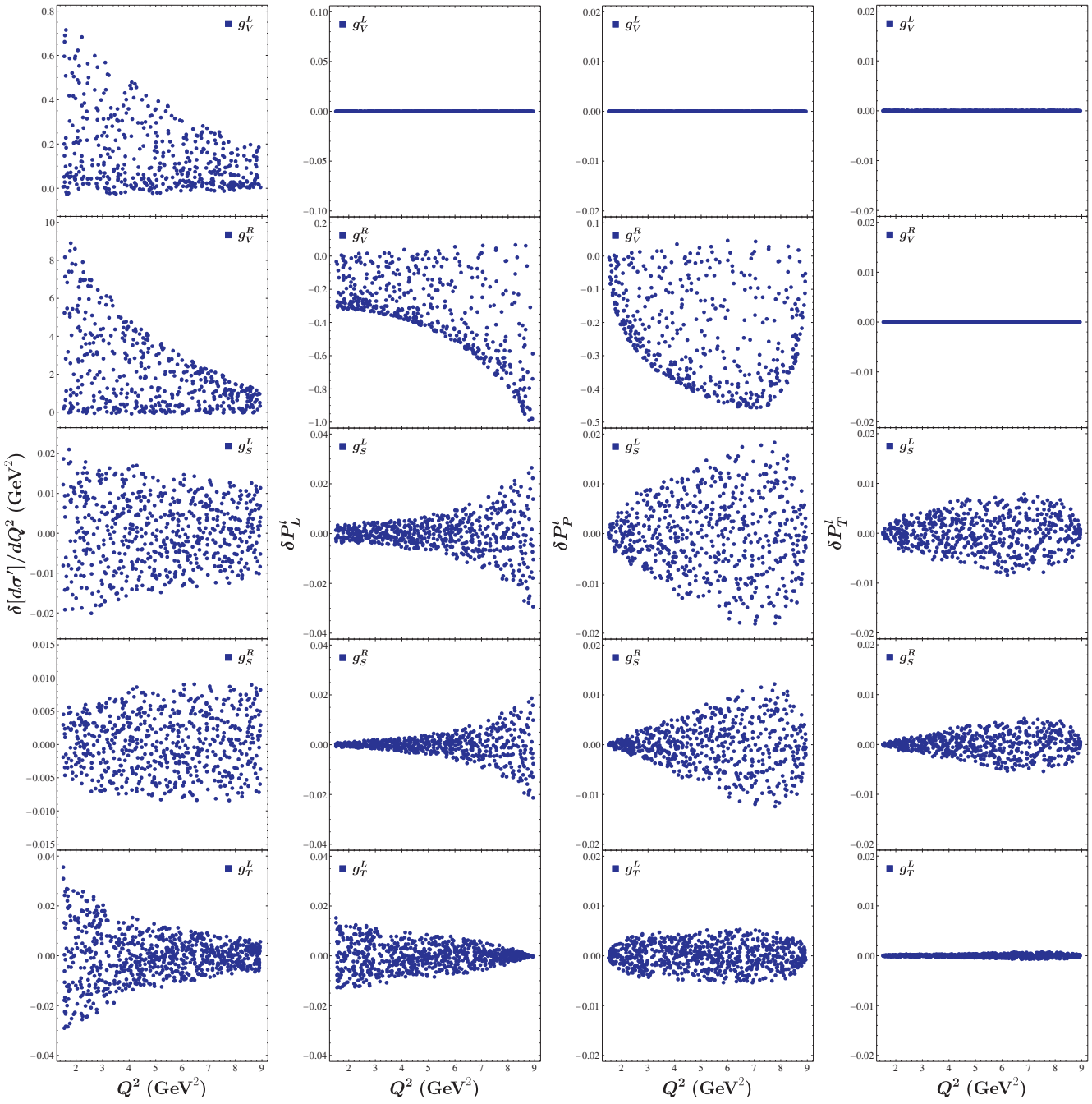

FIG. 7. Deviations from the SM predictions for the differential cross section and the polarizations P_L^l, P_P^l, and P_T^l in different NP scenarios.

Given that only a single nonzero g_i is activated at a time, the two traces in the polarization four-vector $\mathcal{P}^\mu$ [see, e.g., Eq. (12)] can be written, respectively, as

$$\begin{aligned}\mathrm{Tr}[\rho] &= D_{\mathrm{SM}} + (g_i)^* D_{VL,i} + (g_i) D_{VL,i}^* + \mathcal{O}(|g_i|^2) \\ &= D_{\mathrm{SM}} + 2\mathrm{Re}[g_i^* D_{VL,i}] + \mathcal{O}(|g_i|^2), \end{aligned} \tag{24}$$

and

$$\mathrm{Tr}[\rho\gamma^\mu\gamma^5] = \mathcal{N}^\mu_{\mathrm{SM}} + 2\mathrm{Re}[g_i^* \mathcal{N}^\mu_{VL,i}] + \mathcal{O}(|g_i|^2), \tag{25}$$

where D_{SM} and $\mathcal{N}^\mu_{\mathrm{SM}}$ stand for the SM contributions to the two traces $\mathrm{Tr}[\rho]$ and $\mathrm{Tr}[\rho\gamma^\mu\gamma^5]$ respectively, while $D_{VL,i}$ and $\mathcal{N}^\mu_{VL,i}$ denote the contributions to these two traces from the interference between the SM and the NP operator associated with g_i; explicit expressions of the various terms in the two traces can be found in Appendixes B and C.

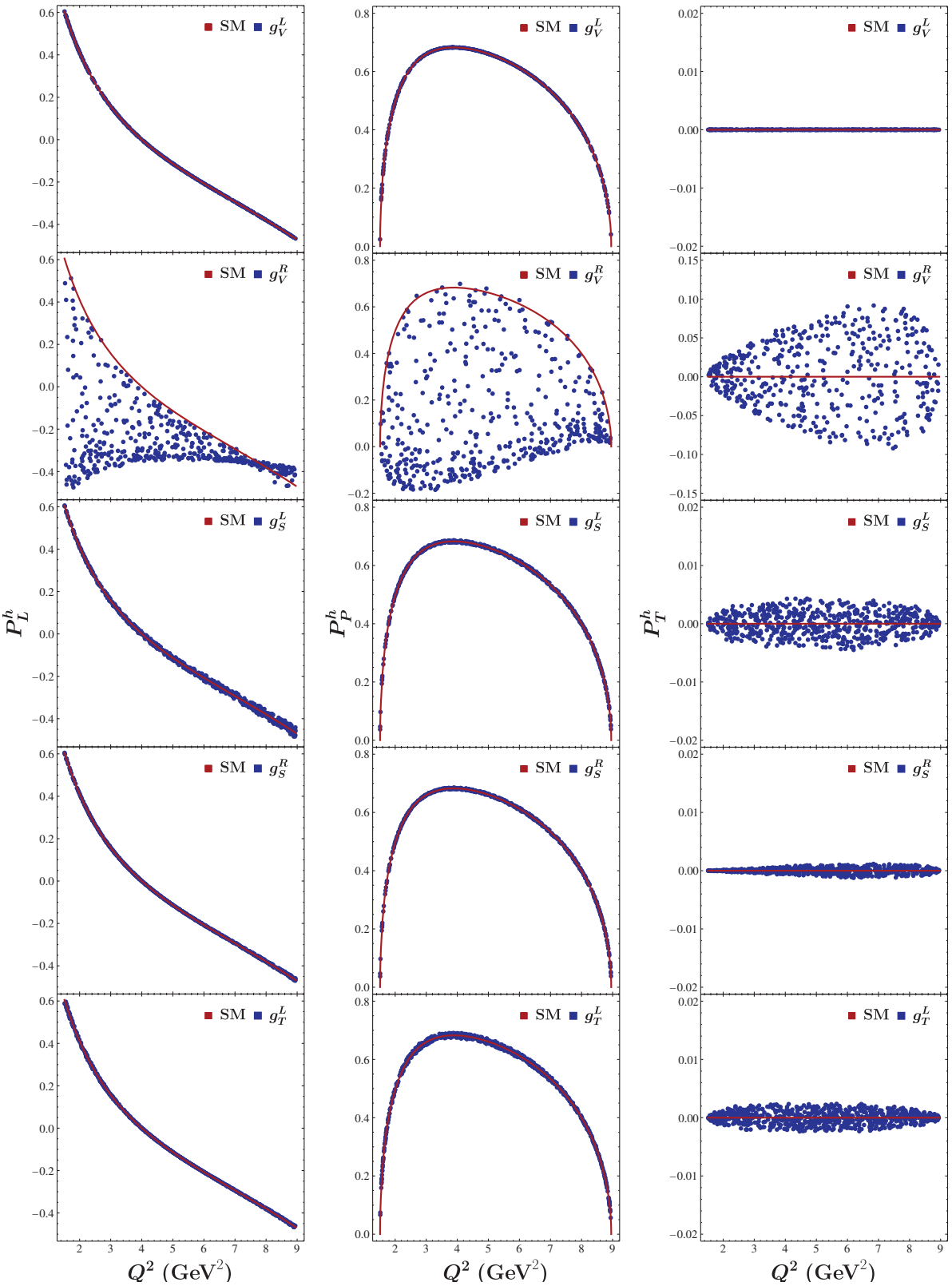

FIG. 8. Variations of the polarizations P_L^h, P_P^h, and P_T^h with respect to Q^2, where the neutrino beam energy has also been set at $E = 10$ GeV for consistency. The color captions are the same as in Fig. 3.

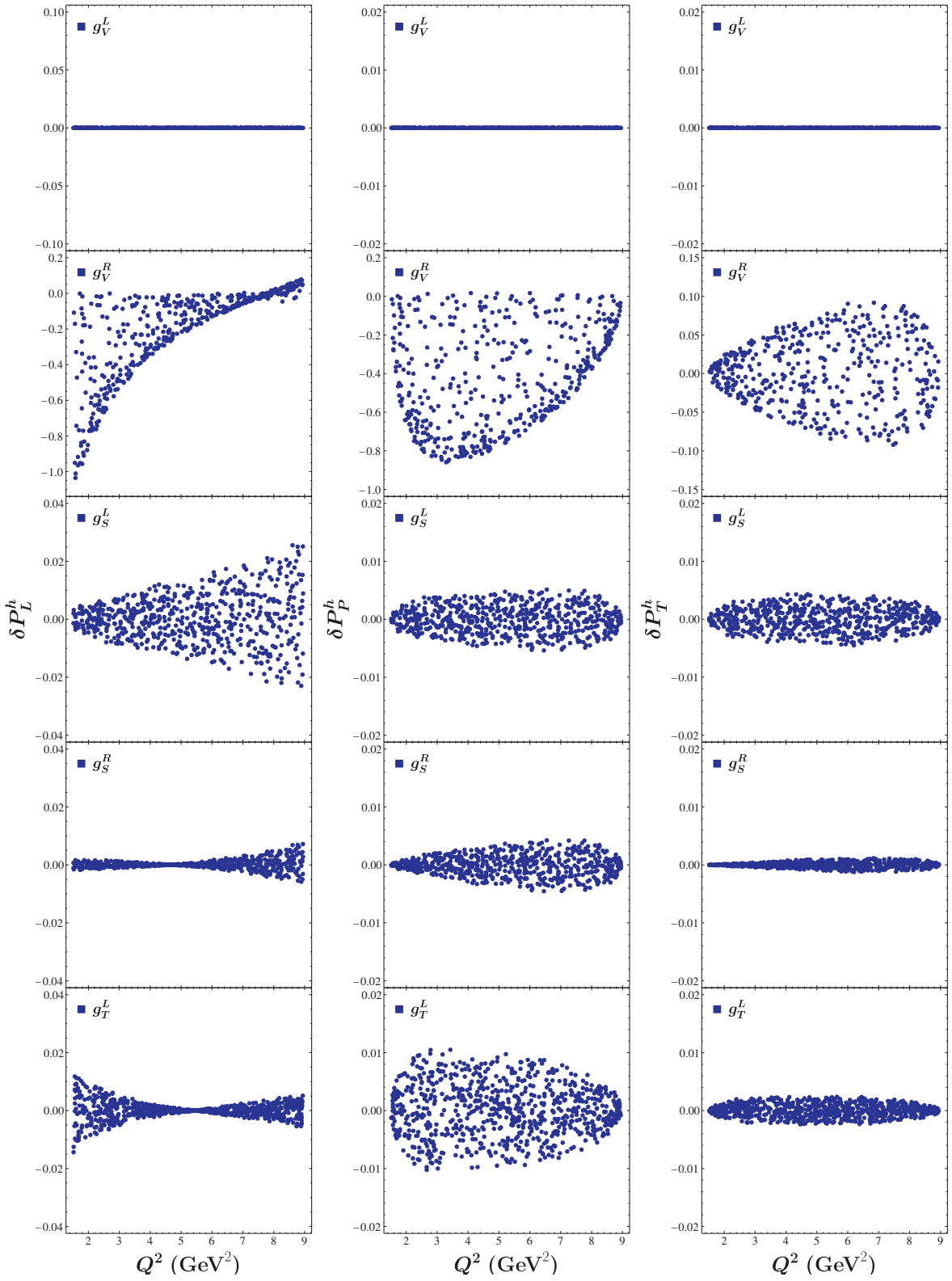

FIG. 9. Deviations from the corresponding SM predictions for the polarizations P_L^h, P_P^h, and P_T^h in different NP scenarios.

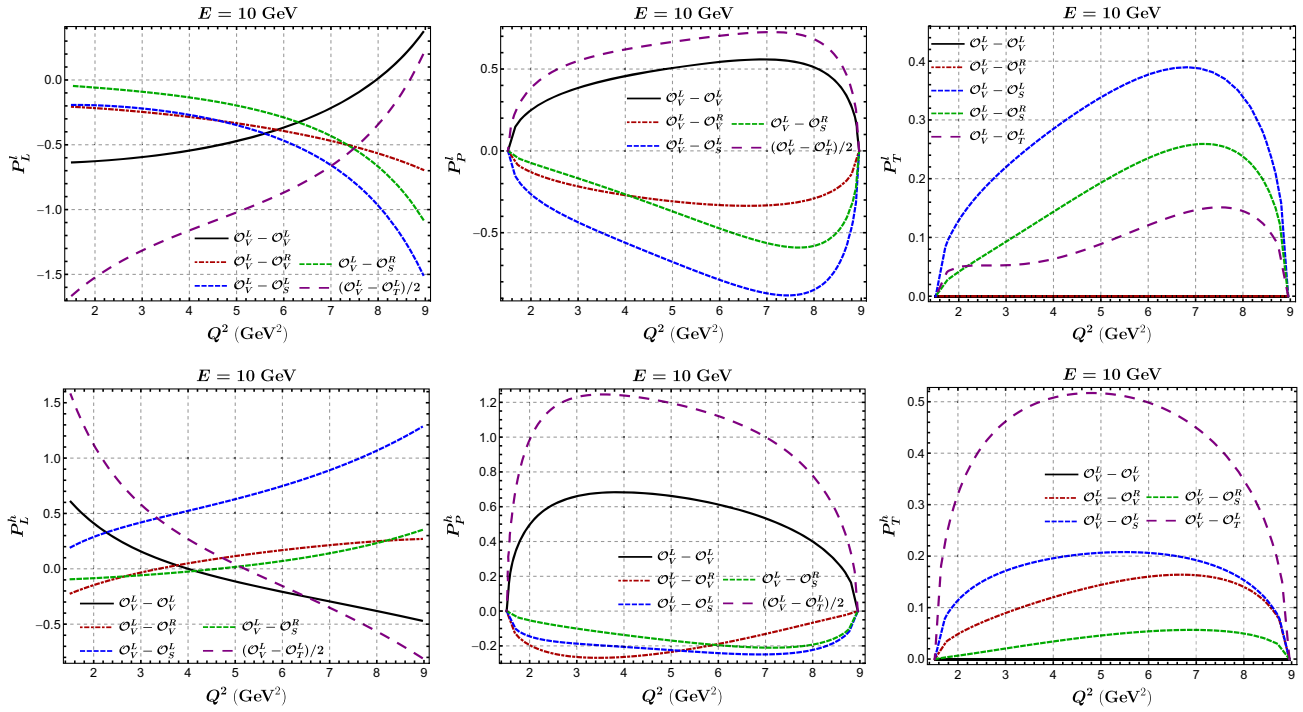

FIG. 10. Variations of $(P_{\rm Int})_a^l$ (top panel) and $(P_{\rm Int})_a^h$ (bottom panel) with respect to Q^2 in different NP scenarios. Note that the mixing $\mathcal{O}_V^L - \mathcal{O}_V^L$ denoted by the solid dark curve represents in fact $(P_{\rm SM})_a^{l,h}$, and the mixing $(\mathcal{O}_V^L - \mathcal{O}_T^L)/2$ indicates that only half of $(P_{\rm Int})_a^{l,h}$ is depicted in this scenario.

Clearly, the pure NP contributions are of $\mathcal{O}(|g_i|^2)$ and can be, therefore, neglected in the small-g_i regions.

The polarization four-vector can now be approximated as

$$\begin{aligned}\mathcal{P}^\mu &\simeq \frac{\mathcal{N}^\mu_{\rm SM} + 2{\rm Re}[g_i^* \mathcal{N}^\mu_{VL,i}]}{D_{\rm SM} + 2{\rm Re}[g_i^* D_{VL,i}]} \\ &\simeq \frac{\mathcal{N}^\mu_{\rm SM}}{D_{\rm SM}} + \frac{2{\rm Re}[g_i^* \mathcal{N}^\mu_{VL,i}]}{D_{\rm SM}} - \frac{2{\rm Re}[g_i^* D_{VL,i}]}{D_{\rm SM}} \frac{\mathcal{N}^\mu_{\rm SM}}{D_{\rm SM}} \\ &= \mathcal{P}^\mu_{\rm SM} + \frac{2{\rm Re}[g_i^* \mathcal{N}^\mu_{VL,i}]}{D_{\rm SM}} - \frac{2{\rm Re}[g_i^* D_{VL,i}]}{D_{\rm SM}} \mathcal{P}^\mu_{\rm SM} \\ &= \mathcal{P}^\mu_{\rm SM} + \mathcal{P}^\mu_{\rm Int}, \end{aligned} \tag{26}$$

where we have ignored all the contributions from the higher-order terms of g_i, and introduced the new polarization four-vector $\mathcal{P}^\mu_{\rm Int}$, with

$$\mathcal{P}^\mu_{\rm Int} \equiv \frac{2{\rm Re}[g_i^* \mathcal{N}^\mu_{VL,i}]}{D_{\rm SM}} - \frac{2{\rm Re}[g_i^* D_{VL,i}]}{D_{\rm SM}} \mathcal{P}^\mu_{\rm SM}, \tag{27}$$

which is induced by the interference between the SM and the NP operator associated with g_i. Projecting $\mathcal{P}^\mu_{\rm SM}$ and $\mathcal{P}^\mu_{\rm Int}$ onto the orthogonal bases [see Eqs. (18) and (19)], we eventually obtain

$$P^{l,h}_{L,P} = (P_{\rm SM})^{l,h}_{L,P} + {\rm Re}[g_i](P_{\rm Int})^{l,h}_{L,P}, \tag{28}$$

$$P^{l,h}_{T} = {\rm Im}[g_i](P_{\rm Int})^{l,h}_{T}, \tag{29}$$

where $(P_{\rm SM})^{l,h}_T = 0$ has been used.

From the definition of $\mathcal{P}^\mu_{\rm Int}$ in Eq. (27), one can already see that $\mathcal{N}^\mu_{VL,VL} = \mathcal{N}^\mu_{\rm SM}$ and $D_{VL,VL} = D_{\rm SM}$ for the g_V^L scenario. Since both $\mathcal{N}^\mu_{\rm SM}$ and $D_{\rm SM}$ are real, $\mathcal{P}^\mu_{\rm Int}$ vanishes, which in turn leads to $P_{\rm Int} = 0$. In other words, it is impossible to distinguish the g_V^L scenario from the SM through the polarization vectors, which has already been observed repetitively in the previous subsections.

We then show in Fig. 10 the variations of $(P_{\rm SM})_a^{l,h}$ and $(P_{\rm Int})_a^{l,h}$ with respect to Q^2 in various NP scenarios, where, for simplicity, we have labeled them by $P_a^{l,h}$ uniformly. From the P_L^l-Q^2 plot (the left-top one in Fig. 10), one can see that $(P_{\rm Int})_L^l$ behave in a very similar way for the g_S^L and g_S^R scenarios, which are denoted by the blue and green dashed curves, respectively. Together with another straightforward observation that the magnitude of $(P_{\rm Int})_L^l$ at any Q^2 in the g_S^L case is always larger than in the g_S^R case, it is expected that the maximum deviation δP_L^l for the g_S^L and g_S^R scenarios must have a similar shape but with the former broader than the latter. Such a behavior has already been observed explicitly in Fig. 7. From the dot-dashed red curve, one can see that, below $Q^2 = 5$ GeV^2, $(P_{\rm Int})_L^l$ for the g_V^R scenario behaves just like that for g_S^L, indicating a similar shape of δP_L^l within this Q^2 range. However, the shape of

δP_L^l will become narrower as Q^2 increases, even narrower than that for the g_S^R scenario at the high-Q^2 range. Such an expectation is, unfortunately, buried by the vast shadow of the δP_L^l-Q^2 plot shown in Fig. 7, due to the large parameter space of g_V^R. Compared with $(P_{\rm SM})_L^l$ denoted by the black curve, the absolute value of $(P_{\rm Int})_L^l$ for the g_T^L scenario (see the long-dashed purple curve) is always larger. However, their difference decreases as Q^2 increases, justifying that a low Q^2 is favored to observe a maximum deviation of δP_L^l in the g_T^L scenario, as shown in Fig. 7.

We now turn to discuss the various curves in the P_P^l-Q^2 plot (the middle-top one in Fig. 10). It can be seen that the blue and green dashed curves behave in a similar way—both peak roughly at $Q^2 = 7.5$ GeV^2—but with different magnitudes. Although the dashed purple curve also peaks at a similar Q^2, it behaves less dramatically within the range $Q^2 \in [3, 7]$ GeV^2. Nonetheless, all of these three curves drop to zero at $Q^2_{\rm min}$ and $Q^2_{\rm max}$. Taking all these points into account, one can understand the interesting features of the deviation δP_P^l observed in the g_S^L, g_S^R, and g_T^L scenarios, as shown in Fig. 7. For the g_V^R scenario, as indicated by the dot-dashed red curve, the deviation δP_P^l shall behave similarly to that for the g_S^R scenario but with a more flattened curvature at the high-Q^2 range. This is different from the behaviors of the deviation δP_L^l in the same NP scenarios, as can be clearly seen from Fig. 7.

Let us move on to the P_L^h-Q^2 plot (the left-bottom one in Fig. 10). A couple of observations can already be made. First, all of the curves except the dashed blue one experience a crossover, indicating that the deviations δP_L^h become zero at a certain Q^2 for the g_V^R, g_S^R, and g_T^L scenarios, while in the g_S^L case δP_L^h increases along with the increase of Q^2. Second, both the green and purple dashed curves cross the $P_L^h = 0$ line at $Q^2 \simeq 5$ GeV^2, suggesting a similar behavior of δP_L^h for the g_S^R and g_T^L scenarios. However, the pattern of small at the $Q^2_{\rm min}$ while relatively large at the $Q^2_{\rm max}$ region of $(P_{\rm Int})_L^h$ reveals that the deviation δP_L^h must be narrower at the $Q^2_{\rm min}$ than at the $Q^2_{\rm max}$ one for the g_S^R scenario. This is contrary to the pattern of δP_L^h observed for the g_T^L scenario, as can be clearly seen from Fig. 9. Finally, the similar behavior between the green and blue dashed curves indicates that the deviation δP_L^h shall behave similarly for the g_V^R and g_S^R scenarios, provided they are both assumed at the small-g_i limit.

With regard to the P_P^h-Q^2 plot (the middle-bottom one in Fig. 10), one can draw some similar observations as from the P_P^l-Q^2 plot. For instance, the similar behavior between the green and blue dashed curves predicts a close shape of δP_P^h for the g_S^L and g_S^R scenarios. The small difference between the resulting values of $(P_{\rm Int})_P^h$, however, suggests that the deviation δP_P^h for the former must be broader than for the latter, as shown in Fig. 9. Meanwhile, the blue and green dashed curves in the P_P^h-Q^2 and P_P^l-Q^2 plots indicate that both δP_P^h and δP_P^l in these two scenarios shall peak at $Q^2 \simeq 7$ GeV^2. Another example is that the red and purple dashed curves reveal that the maximal δP_P^h occurs at low Q^2, $Q^2 \simeq 3.4$ GeV^2, contrary to its counterpart δP_P^l, for the g_L^R and g_T^L scenarios.

We conclude this subsection by giving a brief discussion of the P_T^l-Q^2 and P_T^h-Q^2 plots in Fig. 10. Since the SM contribution to $P_T^{l,h}$ denoted by the dark line is zero, the shapes of other curves reveal not only the behaviors of the polarizations $P_T^{l,h}$ but also the deviations $\delta P_T^{l,h}$ directly. It can be seen that the blue, green, and purple dashed curves in the P_T^l-Q^2 plot behave similarly in general with only some small differences, indicating a similar pattern of the deviation δP_T^l for the g_S^L, g_S^R, and g_T^L scenarios. The blue, green, and purple dashed curves in the P_T^h-Q^2 plot, on the other hand, behave quite differently in both their curvatures and peak positions, justifying the distinct shapes of δP_T^h for the g_S^L, g_S^R, and g_T^L scenarios, as shown in Fig. 9. Finally, the deviation δP_T^h for the g_V^R scenario in Fig. 9 behaves just like the dashed red curve in Fig. 10, even though the latter works only in the small-g_i limit.

D. Observables with uncertainties due to the form factors

As mentioned in Sec. II B, one of the reasons that we adopt the LQCD calculations of the $\Lambda_c \to N$ transition form factors is that they provide us with an error estimation. Yet our calculation has only involved the central values of these inputs so far. In this subsection, we study how our predictions of the observables are affected by the uncertainties of these form factors. As a simple illustration, we focus on the NP scenarios in the presence of the WCs g_V^R and g_S^R, and consider only the Q^2-dependent observables, i.e., the differential cross section and the polarizations $P_a^{l,h}$. To this end, we first scan randomly g_V^R and g_S^R within the available parameter space shown in Fig. 2 and propagate the uncertainties of the form factors to each observable for all the allowed data points of g_V^R and g_S^R. We then plot in Figs. 11 and 12 the central, upper, and lower values of each observable in blue, green, and red accordingly, instead of presenting them in error bars. In this way, the combined regions of the green and red ones as well as the regions between them can be naively understood as the overall uncertainty of the observable considered.

From Figs. 11 and 12, we see that there exist large overlaps among the three colored regions in the low-Q^2 region for each observable in the g_V^R scenario, indicating that the dominant factor determining the overall shape of these observables is still due to the vast available parameter space of g_V^R. But the impact from the uncertainties of the form factors becomes gradually distinct, particularly in the relatively high-Q^2 region where the uncertainty from the form factors for each observable can more than double.

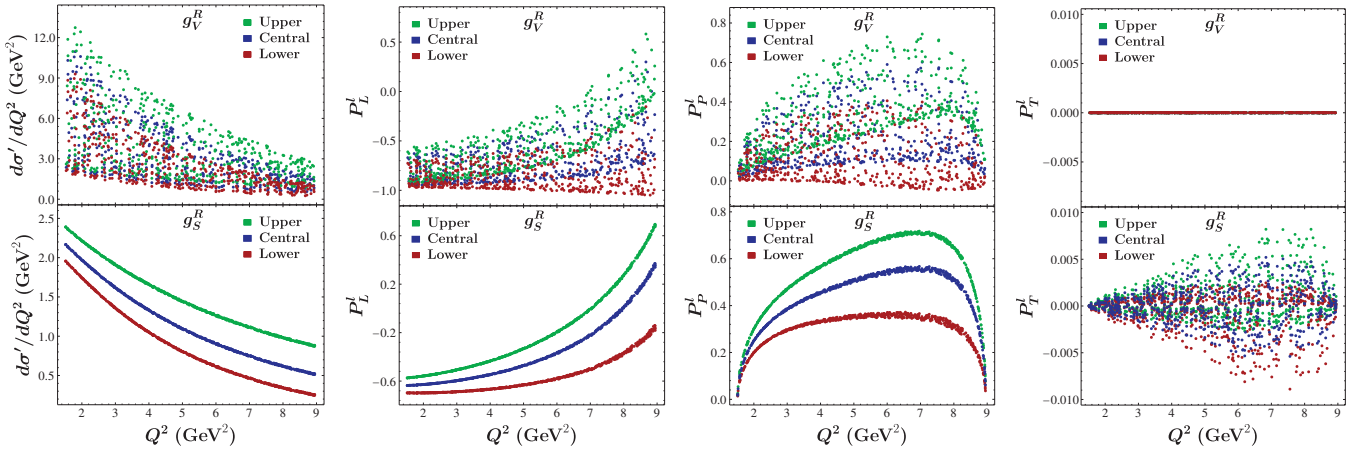

FIG. 11. Uncertainties of the differential cross section as well as the polarizations P_L^l, P_P^l, and P_T^l due to the $\Lambda_c \to N$ transition form factors, in the g_V^R (top panel) and g_S^R (bottom panel) scenarios. The blue points denote the resulting observables calculated with the central values, whereas the green (red) points the observables computed with the upper (lower) values at 1σ level of these form factors. Note that the neutrino beam energy has been fixed at $E = 10$ GeV for consistency.

As for the g_S^R scenario, the large blank spaces between the blue and green (red) regions represent the impacts on the observables from the uncertainties of the form factors, which clearly dwarf the effect of the WC g_S^R due to the stringent experimental constraint on it. The only exceptions are P_T^l and P_T^h in both NP scenarios, on which the impacts from the uncertainties of the form factors and the available parameter space of the WCs seem comparable. These observations can be easily applied to other NP scenarios too.

Besides the above comparisons, it may be also interesting to explore how the uncertainties of the observables propagate along the kinematics Q^2. To this end, let us focus on the observables in the g_S^R scenario as an illustration. First, the green and red regions on the bottom panel of Figs. 11 and 12 clearly indicate that the overall uncertainties of the differential cross section and the polarizations $P_L^{l,h}$ increase along with the increase of Q^2. Second, the uncertainties of $P_P^{l,h}$ and $P_T^{l,h}$ shrink at the $Q^2_{\rm min}$ and $Q^2_{\rm max}$ regions, mainly due to the characteristic behaviors of $P_P^{l,h}$ and $P_T^{l,h}$, but the general pattern is still consistent with what we have just observed. Such a pattern is closely related to the behaviors of the form factors with respect to Q^2. As can be seen from Fig. 16, the uncertainties of all the form factors follow the same pattern as the observables do—the total uncertainties in particular increase dramatically along with the increase of Q^2. Because of the relatively milder behaviors of the statistical uncertainties, we take them instead of the total uncertainties into account in Figs. 11 and 12, as well as in the rest of this work.

In short, although the LQCD calculation [30] of the $\Lambda_c \to N$ transition form factors comes with an error estimation—one of its advantages over the model evaluations presented in Refs. [55–57], the persistently increasing uncertainties along with the increase of Q^2 have

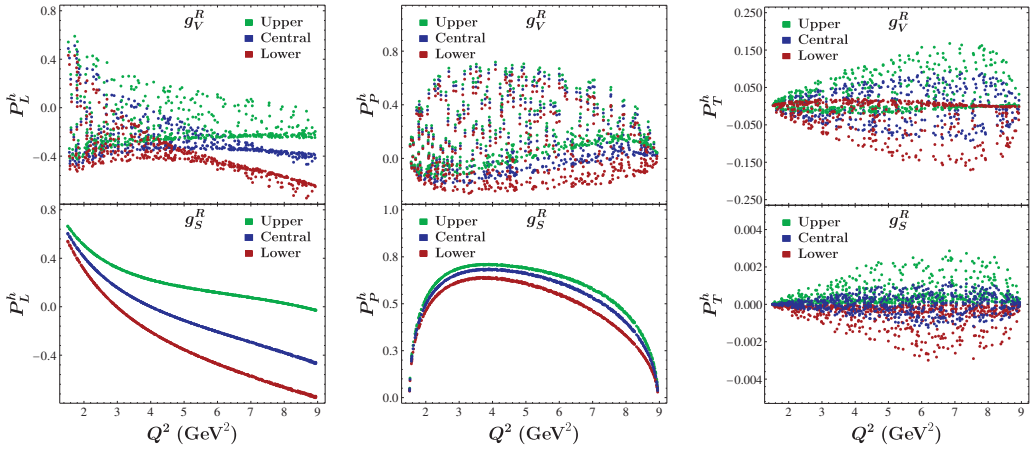

FIG. 12. Uncertainties of the polarizations P_L^h, P_P^h, and P_T^h due to the $\Lambda_c \to N$ transition form factors, in the g_V^R (top panel) and g_S^R (bottom panel) scenarios. The other captions are the same as in Fig. 11.

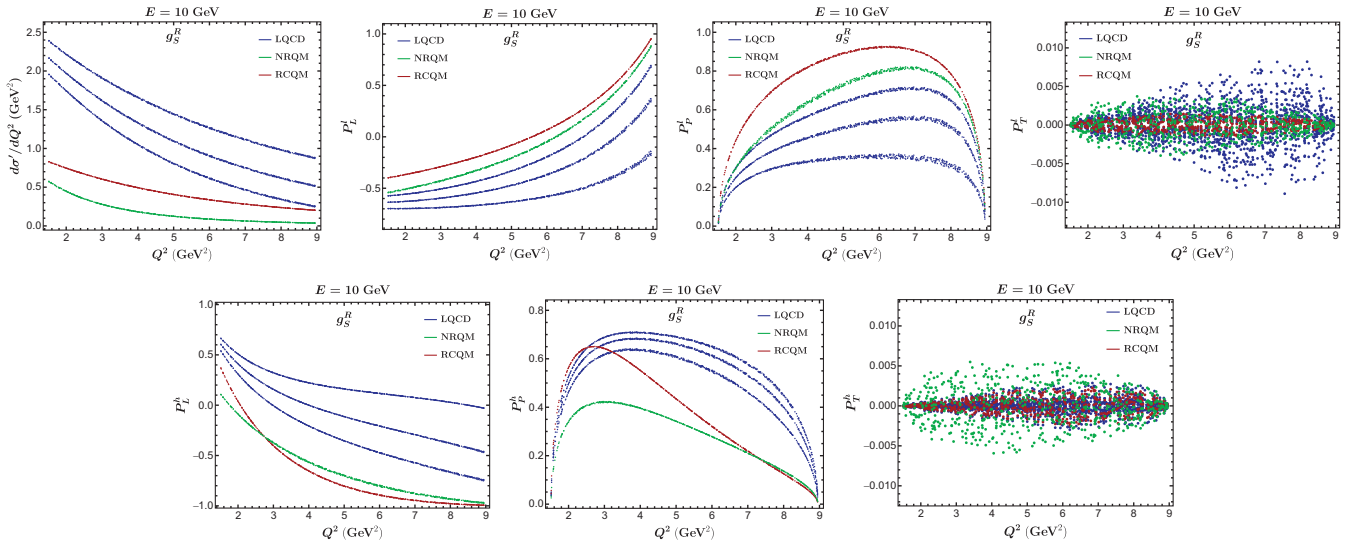

FIG. 13. The differential cross section as well as the polarizations $P_L^{l,h}$, $P_P^{l,h}$, and $P_T^{l,h}$ as a function of Q^2, predicted with the form factors calculated in LQCD (blue), NRQM (green), and RCQM (red), respectively. Here we focus only on the g_S^R scenario. Note that the 1σ-level statistical uncertainties of the form factors in LQCD have been propagated to all the observables, as denoted by the outer blue regions.

become one of the major obstacles to further probe or constrain the NP scenarios through the QE neutrino scattering process. This calls for either better control of the uncertainties of the form factors in future LQCD calculations or new model estimations of these form factors with a good error estimation within the relevant kinematic ranges.

E. Observables with different form-factor parametrizations

The parametrization scheme adopted in Ref. [30] is not the only way to describe the q^2 dependence of the $\Lambda_c \to N$ transition form factors; nor is the LQCD the only method for evaluating the form factors. As discussed in Sec. II B and detailed in Appendix A, there exist already three different parametrization schemes, which can be extended to the $q^2 < 0$ range, and have been employed by the MBM, NRQM, and RCQM models, as well as the LQCD calculations. Moreover, these parametrization schemes are validated against the experimental measurements of the Λ_c semileptonic decays reported by the BESIII Collaboration [58,59].[4] However, direct calculations of the QE weak production of the Λ_c baryon through the ν_μ scattering off nuclei reveal that large deviations arise by using the different schemes of the form factors, demonstrating a direct consequence of the ambiguities induced by extrapolating the form factors to the moderately large positive Q^2 [29]. Given that our analysis is based on the same extrapolation, we examine in this subsection if the same observation applies to the observables considered here in various NP scenarios.

In Fig. 13, we evaluate the differential cross section and the polarizations $P_a^{l,h}$ with the form factors calculated in LQCD (blue), NRQM (green), and RCQM (red), respectively.[5] To be thorough, we also take account of the 1σ-level statistical uncertainties of the form factors in the LQCD case. As an illustration, we focus only on the NP scenario in the presence of g_S^R. From Fig. 13, it can be seen that there exists large disparity between the red (green) and blue regions, indicating that the resulting deviations of $d\sigma$, $P_L^{l,h}$, and $P_P^{l,h}$ due to the different parametrization schemes of the form factors dwarf that from the 1σ-level statistical uncertainties of the form factors in LQCD. For the polarization P_T^l, on the other hand, the overall blue region prevails over the others, indicating a totally opposite situation. Finally, comparing the red region with the overall blue one in the P_T^h-Q^2 plot, one can see that the deviation of P_T^h in RCQM from the LQCD predication can be comparable to that from the 1σ-level statistical uncertainties of the form factors in LQCD.

The SM predictions of $(P_{\rm Int})_a^l$ and $(P_{\rm Int})_a^h$ are presented in the first columns of Figs. 14 and 15, respectively. One can see that among the three cases, the LQCD predicts the largest differential cross section of the QE scattering

[4]Note that the BESIII collaboration has improved the measurement of the absolute branching fraction of $\Lambda_c^+ \to \Lambda e^+ \nu_e$ decay [60].

[5]We do not present the results with the form factors calculated in MBM, because both MBM and NRQM employ the dipole form for the q^2 dependence of the form factors [55,56] (see Appendix A for details).

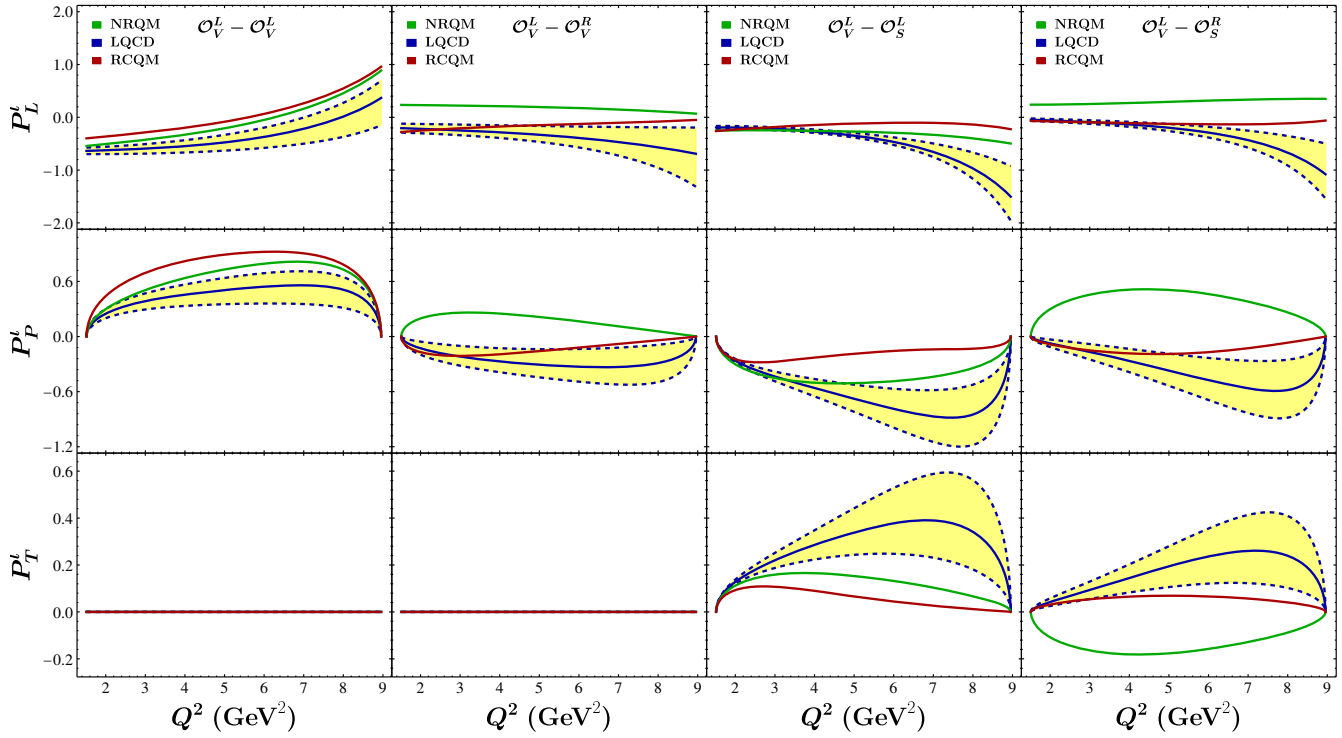

FIG. 14. Variations of $(P_{\rm Int})_a^l$ with respect to Q^2 in various NP scenarios, as predicted with the form factors calculated in LQCD (blue), NRQM (green), and RCQM (red), respectively. The 1σ-level statistical uncertainties of the form factors in LQCD have been propagated to $(P_{\rm Int})_a^l$, as denoted by the yellow region. The neutrino beam energy has been set to $E = 10$ GeV.

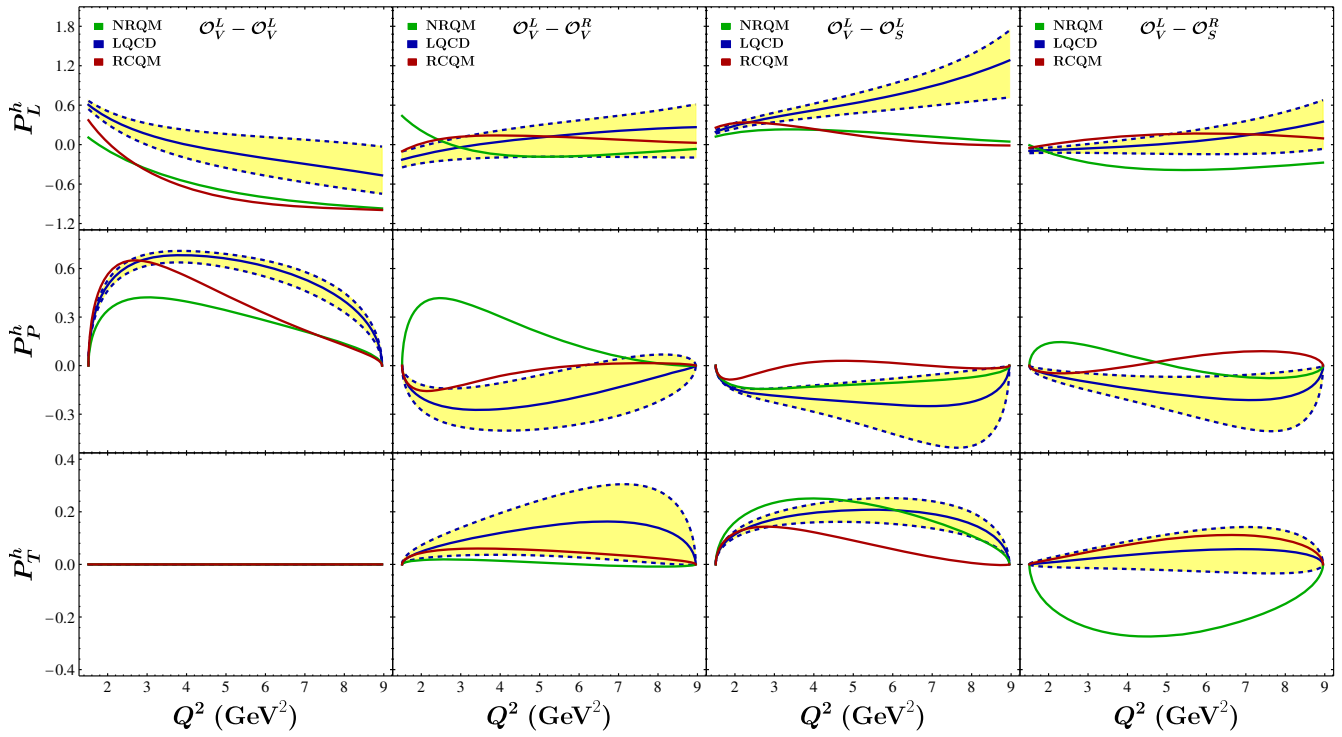

FIG. 15. Variations of $(P_{\rm Int})_a^h$ with respect to Q^2 in various NP scenarios, as predicted with the form factors calculated in LQCD (blue), NRQM (green), and RCQM (red), respectively. The other captions are the same as in Fig. 14.

process in the SM, while the NRQM yields the smallest. Such a pattern is also consistent with that observed in the QE weak production of the Λ_c baryon through the process $\nu_\mu + {}^{16}\mathrm{O} \to \mu^- + \Lambda_c + X$ [29]. However, the situation becomes more complicated for other observables. For instance, the crossover behavior of $P_L^{l,h}$ makes the $P_L^{l,h} = 0$ line a watershed: above it the RCQM (LQCD) predicts the largest P_L^l (P_L^h), while below it the LQCD (RCQM) predicts the largest P_L^l (P_L^h). In addition, the RCQM always seems to produce a larger $P_P^{l,h}$ than the NRQM does.

The small width of each fuzzy colored region in Fig. 13 results from the variation of the WC g_S^R within the allowed parameter space shown in Fig. 2. To have a clearer view of this effect, we work in the small-g_i limit and plot in Figs. 14 and 15 the variations of $(P_{\mathrm{SM}})_a^{l,h}$ and $(P_{\mathrm{Int}})_a^{l,h}$ with respect to Q^2 with the form factors calculated in LQCD (blue), NRQM (green), and RCQM (red), both within the SM and in the g_V^R, g_S^L, and g_S^R scenarios. Note that the g_T^L scenario is not considered here, because the relevant tensor form factors have not been calculated in NRQM and RCQM. Once again, the 1σ-level statistical uncertainties of the form factors have been taken into account in the LQCD case (see the yellow regions shown in Figs. 14 and 15).

Since the resulting $P_a^{l,h}$ due to the mixing $\mathcal{O}_V^L$-$\mathcal{O}_V^L$ correspond exactly to the SM case, which has been discussed above, let us now move on to the next three mixing scenarios. For the mixing $\mathcal{O}_V^L$-$\mathcal{O}_V^R$, it can be seen that, contrary to $(P_{\mathrm{Int}})_T^h$, the resulting $(P_{\mathrm{Int}})_{L,P}^{l,h}$ from NRQM and RCQM are opposite in sign. At the same time, the absolute values of all the $(P_{\mathrm{Int}})_a^{l,h}$ in these two models are compatible with the LQCD results at the 1σ level. These observations can be applied to the mixing $\mathcal{O}_V^L$-$\mathcal{O}_S^R$ as well, except that the NRQM forecasts the largest absolute value of $(P_{\mathrm{Int}})_T^{l,h}$. For the mixing $\mathcal{O}_V^L - \mathcal{O}_S^L$, on the other hand, one can see that the RCQM always predicts the smallest absolute values of all the $(P_{\mathrm{Int}})_a^{l,h}$, while the NRQM results are in general compatible with that of the LQCD at the 1σ level.

All in all, despite the complicated behaviors of each polarization observable calculated with various form-factor parametrization schemes in different scenarios, an overall observation is that the uncertainties of the polarization observables due to the different schemes even overwhelm that from the error propagation of the statistical uncertainties of the form factors.

IV. CONCLUSION

The absence of semitauonic decays of charmed hadrons makes the decay processes mediated by the quark-level $c \to d\tau^+\nu_\tau$ transition inadequate for probing a generic NP with all kinds of Dirac structures. To fill in this gap, we have considered in this paper the QE neutrino scattering process $\nu_\tau + n \to \tau^- + \Lambda_c$, and proposed searching for NP through the polarizations of the τ lepton and the Λ_c baryon. Working in the framework of a general low-energy effective Lagrangian given by Eq. (3) and using the combined constraints from the measured branching fraction of the purely leptonic $D^+ \to \tau^+\nu_\tau$ decay and the analysis of the high-p_T dilepton invariant mass tails in $pp \to \tau\nu_\tau$ processes, we have performed a comprehensive analysis of the (differential) cross sections and polarization vectors of the $\nu_\tau + n \to \tau^- + \Lambda_c$ process both within the SM and in various NP scenarios.

For the SM, we have shown that the dominant polarization mode of the outgoing τ lepton is longitudinal and that of the Λ_c baryon is perpendicular, whereas the transverse polarizations $\langle P_T \rangle$ of both the τ and Λ_c remain zero in such a QE scattering process. We have also explored the variations of the polarization vectors with respect to the kinematics Q^2, and observed that both P_L^l and P_L^h experience a crossover, and the peaks of P_P^l and P_P^h are both reached within the available kinematic range, though happening at different Q^2 points.

For the various NP scenarios, the overall observation we have made is that, due to the stringent experimental constraints on the WCs g_S^L, g_S^R, and g_T^L, there exist only small [of $\mathcal{O}(10^{-2})$] deviations between the SM and the g_S^L, g_S^R, and g_T^L scenarios for the polarizations $P_a^{l,h}$. By contrast, the larger available parameter space of the WC g_V^R makes all the deviations $\delta P_a^{l,h}$ much bigger, except for δP_T^l which remains zero. As for the g_V^L scenario, since it shares the same effective operator $\mathcal{O}_V^L$ with the SM, all the deviations $\delta P_a^{l,h}$ always remain zero, making the (differential) cross section the only avenue to probe g_V^L through the QE scattering process.

We have also explored the impacts of the uncertainties of the $\Lambda_c \to N$ transition form factors, and shown that they have become one of the major challenges to further probe or constrain the NP scenarios through the QE neutrino scattering process. Furthermore, we have considered three different form-factor parametrization schemes employed by NRQM, RCQM, and LQCD respectively, and discovered large differences among their predictions in the SM, which is also consistent with the observation made in the QE weak production of the Λ_c baryon through the ν_μ scattering off nuclei [29]. For the NP scenarios, although the deviations $\delta P_a^{l,h}$ predicted in NRQM and RCQM are still compatible with the LQCD results at the 1σ level, the overall observation is that large uncertainties of the polarization observables arise from using the different schemes and dwarf that from the error propagation of the form factors, which demonstrates a direct consequence of the ambiguities induced by extrapolating the form factors to the large positive Q^2.

Finally, we would like to make a comment on the detection of the outgoing τ lepton. It is known that the τ lepton decays rapidly and its decay products contain at least

one undetected neutrino, making its identification very challenging and its polarization states hard to be measured. However, its kinematic and polarization information can be inferred from the visible final-state kinematics in its subsequent decays [61–71]. In our upcoming work, we will incorporate this idea into our further analysis of the QE scattering process.

ACKNOWLEDGMENTS

This work is supported by the National Natural Science Foundation of China under Grants No. 12135006 and No. 12075097, the Fundamental Research Funds for the Central Universities under Grants No. CCNU22LJ004 and No. CCNU19TD012, as well as the Pingyuan Scholars Program under Grant No. 5101029470306.

APPENDIX A: DEFINITIONS AND PARAMETRIZATIONS OF THE $\Lambda_c \to N$ TRANSITION FORM FACTORS

The $\Lambda_c \to N$ transition form factors used in this work are defined in the helicity basis [30,32,33]. For the vector and axial-vector currents, their hadronic matrix elements are defined, respectively, by

$$\begin{aligned}&\langle N(p,s)|\bar{d}\gamma^\mu c|\Lambda_c(p',s')\rangle\\&=\bar{u}_N(p,s)\left[f_0(q^2)(m_{\Lambda_c}-m_N)\frac{q^\mu}{q^2}\right.\\&+f_+(q^2)\frac{m_{\Lambda_c}+m_N}{s_+}\left(p'^\mu+p^\mu-(m_{\Lambda_c}^2-m_N^2)\frac{q^\mu}{q^2}\right)\\&\left.+f_\perp(q^2)\left(\gamma^\mu-\frac{2m_N}{s_+}p'^\mu-\frac{2m_{\Lambda_c}}{s_+}p^\mu\right)\right]u_{\Lambda_c}(p',s'),\end{aligned}\tag{A1}$$

and

$$\begin{aligned}&\langle N(p,s)|\bar{d}\gamma^\mu\gamma^5 c|\Lambda_c(p',s')\rangle\\&=-\bar{u}_N(p,s)\gamma^5\left[g_0(q^2)(m_{\Lambda_c}+m_N)\frac{q^\mu}{q^2}\right.\\&+g_+(q^2)\frac{m_{\Lambda_c}-m_N}{s_-}\left(p'^\mu+p^\mu-(m_{\Lambda_c}^2-m_N^2)\frac{q^\mu}{q^2}\right)\\&\left.+g_\perp(q^2)\left(\gamma^\mu+\frac{2m_N}{s_-}p'^\mu-\frac{2m_{\Lambda_c}}{s_-}p^\mu\right)\right]u_{\Lambda_c}(p',s'),\end{aligned}\tag{A2}$$

where $q=p'-p$ and $s_\pm=(m_{\Lambda_c}\pm m_N)^2-q^2$. From Eqs. (A1) and (A2), we can obtain the hadronic matrix elements of the scalar and pseudoscalar currents through the equation of motion, which are given, respectively, by

$$\begin{aligned}&\langle N(p,s)|\bar{d}c|\Lambda_c(p',s')\rangle\\&=\frac{(m_{\Lambda_c}-m_N)}{m_c-m_d}f_0(q^2)\bar{u}_N(p,s)u_{\Lambda_c}(p',s'),\end{aligned}\tag{A3}$$

$$\begin{aligned}&\langle N(p,s)|\bar{d}\gamma^5 c|\Lambda_c(p',s')\rangle\\&=\frac{(m_{\Lambda_c}+m_N)}{m_c+m_d}g_0(q^2)\bar{u}_N(p,s)\gamma^5 u_{\Lambda_c}(p',s'),\end{aligned}\tag{A4}$$

where $m_{d(c)}$ denotes the $d(c)$-quark running mass. Finally, the hadronic matrix element of the tensor current is given by

$$\begin{aligned}&\langle N(p,s)|\bar{d}i\sigma_{\mu\nu}c|\Lambda_c(p',s')\rangle\\&=\bar{u}_N(p,s)\left[2h_+\frac{p'_\mu p_\nu-p'_\nu p_\mu}{s_+}+h_\perp\left(\frac{m_{\Lambda_c}+m_N}{q^2}\right.\right.\\&\times(q_\mu\gamma_\nu-q_\nu\gamma_\mu)-2\left(\frac{1}{q^2}+\frac{1}{s_+}\right)(p'_\mu p_\nu-p'_\nu p_\mu)\Big)\\&+\tilde{h}_+\left(i\sigma_{\mu\nu}-\frac{2}{s_-}[m_{\Lambda_c}(p_\mu\gamma_\nu-p_\nu\gamma_\mu)-m_N(p'_\mu\gamma_\nu-p'_\nu\gamma_\mu)\right.\\&\left.+p'_\mu p_\nu-p'_\nu p_\mu]\right)+\tilde{h}_\perp\frac{m_{\Lambda_c}-m_N}{q^2 s_-}\left((m_{\Lambda_c}^2-m_N^2-q^2)\right.\\&\times(\gamma_\mu p'_\nu-\gamma_\nu p'_\mu)-(m_{\Lambda_c}^2-m_N^2+q^2)(\gamma_\mu p_\nu-\gamma_\nu p_\mu)\\&\left.\left.+2(m_{\Lambda_c}-m_N)(p'_\mu p_\nu-p'_\nu p_\mu)\right)\right]u_{\Lambda_c}(p',s'),\end{aligned}\tag{A5}$$

where $\sigma_{\mu\nu}=i[\gamma_\mu,\gamma_\nu]/2$.

The parametrization of these $\Lambda_c \to N$ transition form factors calculated in LQCD takes the form [30,39]

$$f(q^2)=\frac{1}{1-q^2/(m_{\rm pole}^f)^2}\sum_{n=0}^{n_{\rm max}}a_n^f[z(q^2)]^n,\tag{A6}$$

with the expansion variable defined by

$$z(q^2)=\frac{\sqrt{t_+-q^2}-\sqrt{t_+-t_0}}{\sqrt{t_+-q^2}+\sqrt{t_+-t_0}},\tag{A7}$$

where $t_+=(m_D+m_\pi)^2$ is set equal to the threshold of $D\pi$ two-particle states, $t_0=(m_{\Lambda_c}-m_N)^2$ determines which value of q^2 gets mapped to $z=0$, and the lowest poles are already factored out before the z expansion, with their quantum numbers and masses listed in Table IV of Ref. [30] for the different form factors. The central values and the statistical uncertainties of $a_{0,1,2}^f$ in Eq. (A6) for different form factors $f(q^2)$ have been evaluated in Ref. [30] by the nominal fit ($n_{\rm max}=2$), while their systematic uncertainties can be obtained by a combined analysis of both the nominal and higher-order ($n_{\rm max}=3$) fits; we refer the readers to Ref. [30] for further details.

In Fig. 16, we depict the central values as well as the statistical and total uncertainties of these form factors with respect to the kinematics Q^2. It can be seen that the yellow

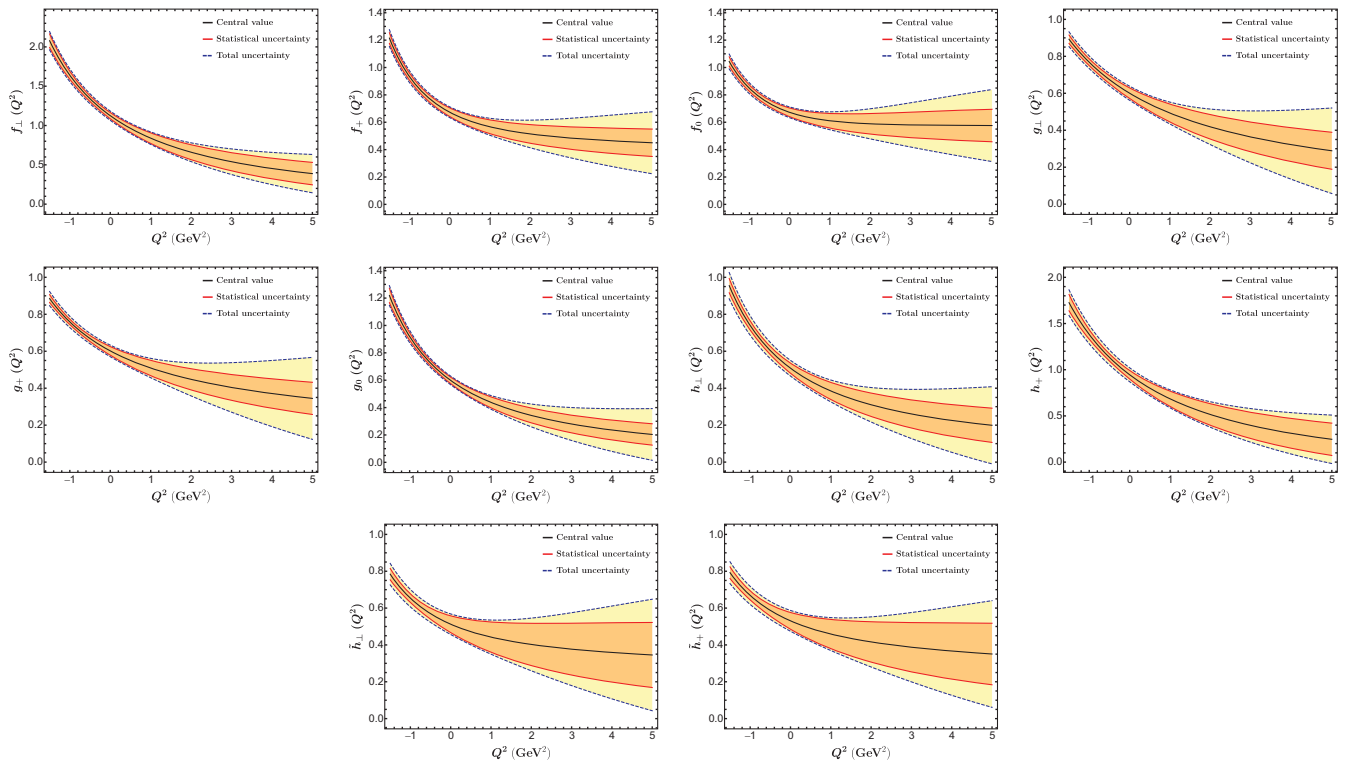

FIG. 16. The Q^2 dependence of the different form factors, where the red and blue dashed lines denote the statistical and total uncertainties of the form factors within 1σ error bars, respectively.

region in each plot increases dramatically along with the increase of Q^2, indicating a larger total uncertainty in the larger Q^2 range. Although the statistical uncertainties also increases along with the increase of Q^2, their behaviors are much milder. Therefore, we only take the statistical uncertainties into account throughout this work.

Often, the hadronic matrix elements of the vector and axial-vector currents are expressed in terms of another set of form factors $f_i^{V,A}$ with $i = 1, 2, 3$, which are related to the ones introduced in Eqs. (A1) and (A2) by

$$\begin{aligned}
f_0 &= \frac{q^2}{m_{\Lambda_c}(m_{\Lambda_c} - m_N)} f_3^V + f_1^V, \\
f_+ &= f_1^V + \frac{q^2}{m_{\Lambda_c}(m_{\Lambda_c} + m_N)} f_2^V, \\
f_\perp &= f_1^V + f_2^V \frac{(m_N + m_{\Lambda_c})}{m_{\Lambda_c}}, \\
g_0 &= -\frac{q^2}{m_{\Lambda_c}(m_{\Lambda_c} - m_N)} f_3^A + f_1^A, \\
g_+ &= f_1^A - \frac{q^2}{m_{\Lambda_c}(m_{\Lambda_c} - m_N)} f_2^A, \\
g_\perp &= f_1^A + f_2^A \frac{(m_N - m_{\Lambda_c})}{m_{\Lambda_c}}.
\end{aligned} \tag{A8}$$

To parametrize the q^2 dependence of this set of form factors, the RCQM model adopts the following double-pole form [57]:

$$f(q^2) = \frac{f(0)}{1 - a\hat{s} + b\hat{s}^2}, \tag{A9}$$

with $\hat{s} = q^2/m_{\Lambda_c}^2$, where the values of the parameters $f(0)$, a, and b are listed in Table II. On the other hand, the MBM and NRQM models employ both the monopole and dipole parametrizations for these form factors [55,56]. For simplicity, we only consider the later, which has the following form:

TABLE II. Values of the parameters employed in Eq. (A9) to construct the q^2 dependence of the form factors associated with the vector and axial-vector currents [see Eqs. (A1) and (A2)] for the RCQM model [57].

	$f(0)$	a	b
f_1^V	0.470	1.111	0.303
f_2^V	0.247	1.240	0.390
f_3^V	0.038	0.308	1.998
f_1^A	0.414	0.978	0.235
f_2^A	−0.073	0.781	0.225
f_3^A	−0.328	1.330	0.486

TABLE III. Values of the parameters employed in Eq. (A10) to construct the q^2 dependence of the form factors associated with the vector and axial-vector currents [see Eqs. (A1) and (A2)] for the MBM and NRQM models [55,56].

	NRQM		MBM	
	A	M_R (GeV)	A	M_R (GeV)
f_1^V	0.22	2.01	0.33	2.01
f_2^V	0.11	2.01	0.18	2.01
f_3^V	0.27	2.01	0.00	2.01
f_1^A	0.58	2.42	0.41	2.42
f_2^A	−0.04	2.42	−0.07	2.42
f_3^A	−0.10	2.42	−0.50	2.42

$$f(q^2) = \frac{A}{(1 - q^2/M_R^2)^2}, \tag{A10}$$

where the values of the parameters A and M_R are reported in Table III. We refer the readers to Ref. [29] for more details about the form-factor parametrizations in different models.

In Fig. 17, we show the Q^2 dependence of these six form factors associated with the matrix elements of the vector and axial-vector currents in the suitable kinematic range ($Q^2 > 0$) for the low-E QE scattering process. It can be seen that the LQCD predicts the largest values for all these six form factors. Especially for f_0, f_+, and g_+, the central values provided by the three models lie outside the 1σ error bars of the LQCD calculations. Interestingly enough, the NRQM model produces the lowest values for $f_{0,+,\perp}$, while the MBM model provides the lowest values for $g_{0,+,\perp}$.

Finally, it should be mentioned that another set of form factors has also been employed to parametrize the transition matrix elements of the vector and axial-vector currents. They can be related to $f_i^{V,A}$ in a trivial way, and have been investigated in the (light-cone) QCD sum rule approach (see, e.g., Refs. [72–74]) and the light-front constituent quark model (see, e.g., Refs. [75,76]). However, since the form factors $f_3^{V,A}$ were not calculated, the results presented in these references will not be considered in this work.

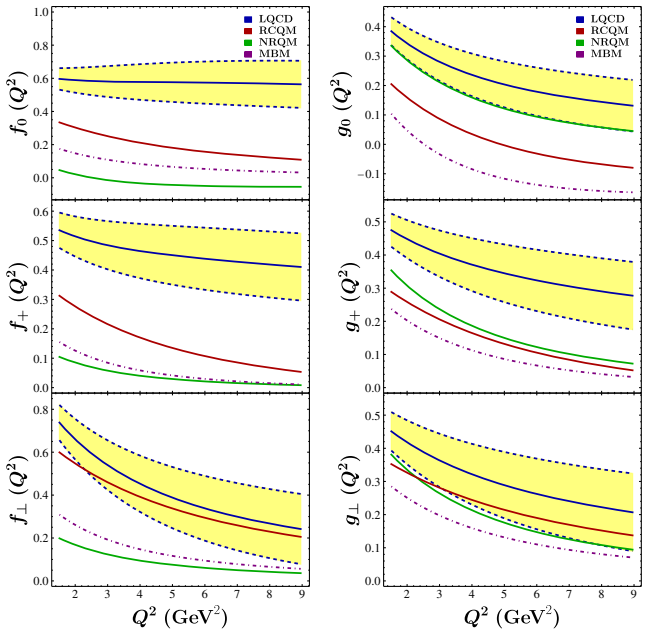

FIG. 17. The Q^2 dependence of the $N \to \Lambda_c$ transition form factors deduced from extrapolating to $Q^2 > 0$ the results of LQCD [30], RCQM [57], NRQM [55,56], and MBM [55,56], respectively.

APPENDIX B: AMPLITUDE SQUARED OF THE QE SCATTERING PROCESS

For the convenience of future discussions, we provide here the explicit expression of the amplitude squared $|\mathcal{M}|^2$ of the QE scattering process $\nu_\tau(k) + n(p) \to \tau^-(k') + \Lambda_c(p')$ mediated by the general effective Lagrangian $\mathcal{L}_{\rm eff}$ [see Eq. (3)]. With all the operators of $\mathcal{L}_{\rm eff}$ taken into account, the amplitude square $|\mathcal{M}|^2$ is given explicitly by

$$\begin{aligned}|\mathcal{M}|^2 = {} & |1 + g_V^L|^2 \mathcal{A}_{V_L - V_L} + |g_V^R|^2 \mathcal{A}_{V_R - V_R} + (|g_S^L|^2 + |g_S^R|^2)\mathcal{A}_{S_L - S_L} + |g_T^L|^2 \mathcal{A}_{T_L - T_L} + 2\mathrm{Re}[g_S^L g_S^{R*}]\mathcal{A}_{S_L - S_R} \\ & + 2\mathrm{Re}[g_V^R(1 + g_V^{L*})]\mathcal{A}_{V_R - V_L} + 2\mathrm{Re}[g_S^L(1 + g_V^{L*}) + g_S^R g_V^{R*}]\mathcal{A}_{S_L - V_L} + 2\mathrm{Re}[g_S^R(1 + g_V^{L*}) + g_S^L g_V^{R*}]\mathcal{A}_{S_R - V_L} \\ & + 2\mathrm{Re}[g_T^L(1 + g_V^{L*})]\mathcal{A}_{T_L - V_L} + 2\mathrm{Re}[g_T^L g_V^{R*}]\mathcal{A}_{T_L - V_R} + 2\mathrm{Re}[g_T^L g_S^{LL*}]\mathcal{A}_{T_L - S_L} + 2\mathrm{Re}[g_T^L g_S^{R*}]\mathcal{A}_{T_L - S_R},\end{aligned} \tag{B1}$$

where the various subscripts attached to the different $\mathcal{A}$ on the right-hand side represent the possible interference between the two operators (see Ref. [24] for more details). Note that, because of the chiral structures of the lepton and quark currents involved, $\mathcal{A}$ with different subscripts can be identical to each other, e.g., $\mathcal{A}_{S_L - V_L} = \mathcal{A}_{S_R - V_R}$ and thus only one of them is kept in Eq. (B1). The amplitudes associated with other interference terms that are not shown in Eq. (B1) are all zero. For convenience, we provide here the explicit expressions of the $\mathcal{A}$ on the right-hand side of Eq. (B1) as

$$\begin{aligned}\mathcal{A}_{V_L - V_L} = {} & \frac{m_\tau^2(m_\tau^2 - q^2)}{2q^4}[f_0^2(m_{\Lambda_c} - m_n)^2 s_+ + g_0^2(m_{\Lambda_c} + m_n)^2 s_-] - \frac{m_\tau^2(m_{\Lambda_c}^2 - m_n^2)}{q^4} \\ & \times (f_0 f_+ + g_0 g_+)[4E m_n q^2 + (m_\tau^2 - q^2)(m_{\Lambda_c}^2 - m_n^2 - q^2)] + \left[\frac{f_+^2(m_{\Lambda_c} + m_n)^2}{2q^4 s_+}\right.\end{aligned}$$

$$+\frac{g_+^2(m_{\Lambda_c}-m_n)^2}{2q^4 s_-}\Big]\Big\{4m_n^2q^4(4E^2-m_\tau^2+q^2)+(m_\tau^2-q^2)(m_{\Lambda_c}^2-m_n^2-q^2)$$
$$\times[8Em_nq^2+m_\tau^2(m_{\Lambda_c}^2-m_n^2-q^2)]\Big\}+\left(\frac{f_\perp^2}{s_+}+\frac{g_\perp^2}{s_-}\right)\Big\{8E^2m_n^2q^2+(m_\tau^2-q^2)$$
$$\times\Big[2m_{\Lambda_c}^2q^2-4Em_n(m_n^2-m_{\Lambda_c}^2+q^2)-(m_{\Lambda_c}^2-m_n^2)^2+2m_n^2m_\tau^2-q^4\Big]\Big\}$$
$$-2f_\perp g_\perp[4Em_nq^2+(m_\tau^2-q^2)(m_{\Lambda_c}^2-m_n^2-q^2)], \tag{B2}$$

$$\mathcal{A}_{V_R-V_R}=\frac{m_\tau^2(m_\tau^2-q^2)}{2q^4}[f_0^2(m_{\Lambda_c}-m_n)^2s_+ + g_0^2(m_{\Lambda_c}+m_p)^2s_-]-\frac{m_\tau^2(m_{\Lambda_c}^2-m_n^2)}{q^4}$$
$$\times(f_0f_+ + g_0g_+)[4Em_nq^2+(m_\tau^2-q^2)(m_{\Lambda_c}^2-m_n^2-q^2)]+\Big[\frac{f_+^2(m_{\Lambda_c}+m_n)^2}{2q^4s_+}$$
$$+\frac{g_+^2(m_{\Lambda_c}-m_n)^2}{2q^4s_-}\Big]\Big\{4m_n^2q^4(4E^2-m_\tau^2+q^2)+(m_\tau^2-q^2)(m_{\Lambda_c}^2-m_p^2-q^2)$$
$$\times[8Em_nq^2+m_\tau^2(m_{\Lambda_c}^2-m_n^2-q^2)]\Big\}+\left(\frac{f_\perp^2}{s_+}+\frac{g_\perp^2}{s_-}\right)\Big\{8E^2m_n^2q^2+(m_\tau^2-q^2)$$
$$\times\Big[2m_{\Lambda_c}^2q^2-4Em_n(m_n^2-m_{\Lambda_c}^2+q^2)-(m_{\Lambda_c}^2-m_n^2)^2+2m_n^2m_\tau^2-q^4\Big]\Big\}$$
$$+2f_\perp g_\perp[4Em_nq^2+(m_\tau^2-q^2)(m_{\Lambda_c}^2-m_n^2-q^2)], \tag{B3}$$

$$\mathcal{A}_{S_L-S_L}=\frac{m_\tau^2-q^2}{2m_c^2}[f_0^2(m_{\Lambda_c}-m_n)^2s_+ + g_0^2(m_{\Lambda_c}+m_n)^2s_-], \tag{B4}$$

$$\mathcal{A}_{T_L-T_L}=-8\left(\frac{h_+^2}{s_+}+\frac{\tilde{h}_+^2}{s_-}\right)\Big\{4m_\tau^4m_n^2+m_{\Lambda_c}^4(q^2-m_\tau^2)+2m_{\Lambda_c}^2(m_\tau^2-q^2)(4Em_n+m_n^2$$
$$+q^2)+q^2(4Em_n+m_n^2+q^2)^2-m_\tau^2[m_n^4+6m_n^2q^2+q^4+8Em_n(m_n^2+q^2)]\Big\}$$
$$+16\left[\frac{h_\perp^2(m_{\Lambda_c}+m_n)^2}{s_+q^4}+\frac{\tilde{h}_\perp^2(m_{\Lambda_c}-m_n)^2}{s_-q^4}\right]\Big\{2m_n(2E+m_n)q^4(2Em_n+q^2)$$
$$-m_\tau^2q^2(m_n^2+q^2)(4Em_n+m_n^2+q^2)+m_{\Lambda_c}^4m_\tau^2(m_\tau^2-q^2)+m_\tau^4(m_n^4+q^4)$$
$$-2m_{\Lambda_c}^2(m_\tau^2-q^2)[m_\tau^2(m_n^2+q^2)-2Em_nq^2]\Big\}-\frac{32m_\tau^2(m_{\Lambda_c}^2-m_n^2)}{q^4}$$
$$\times[m_{\Lambda_c}^2(m_\tau^2-q^2)-m_\tau^2(m_n^2+q^2)+q^2(4Em_n+m_n^2+q^2)]h_\perp\tilde{h}_\perp, \tag{B5}$$

$$\mathcal{A}_{V_R-V_L}=\frac{m_\tau^2(m_\tau^2-q^2)}{2q^4}[f_0^2(m_{\Lambda_c}-m_n)^2s_+ - g_0^2(m_{\Lambda_c}+m_n)^2s_-]-\frac{m_\tau^2(m_{\Lambda_c}^2-m_n^2)}{q^4}$$
$$\times(f_0f_+ - g_0g_+)[4Em_nq^2+(m_\tau^2-q^2)(m_{\Lambda_c}^2-m_n^2-q^2)]+\Big[\frac{f_+^2(m_{\Lambda_c}+m_n)^2}{2q^4s_+}$$
$$-\frac{g_+^2(m_{\Lambda_c}-m_n)^2}{2q^4s_-}\Big]\Big\{4m_n^2q^4(4E^2-m_\tau^2+q^2)+(m_\tau^2-q^2)(m_{\Lambda_c}^2-m_n^2-q^2)$$
$$\times[8Em_nq^2+m_\tau^2(m_{\Lambda_c}^2-m_n^2-q^2)]\Big\}+\left(\frac{f_\perp^2}{s_+}-\frac{g_\perp^2}{s_-}\right)\{8E^2m_n^2q^2+(m_\tau^2-q^2)$$
$$\times[2m_{\Lambda_c}^2q^2-4Em_n(m_n^2-m_{\Lambda_c}^2+q^2)-(m_{\Lambda_c}^2-m_n^2)^2+2m_n^2m_\tau^2-q^4]\}, \tag{B6}$$

$$\mathcal{A}_{S_L-V_L}=\frac{m_\tau(q^2-m_\tau^2)}{2m_c q^2}[f_0^2(m_{\Lambda_c}-m_n)^2 s_+ + g_0^2(m_{\Lambda_c}+m_n)^2 s_-]+\frac{m_\tau(m_{\Lambda_c}^2-m_n^2)}{2m_c q^2}\times(f_0 f_+ + g_0 g_+)[4Em_n q^2+(m_\tau^2-q^2)(m_{\Lambda_c}^2-m_n^2-q^2)], \tag{B7}$$

$$\mathcal{A}_{S_R-V_L}=\frac{m_\tau(q^2-m_\tau^2)}{2m_c q^2}[f_0^2(m_{\Lambda_c}-m_n)^2 s_+ - g_0^2(m_{\Lambda_c}+m_n)^2 s_-]+\frac{m_\tau(m_{\Lambda_c}^2-m_n^2)}{2m_c q^2}\times(f_0 f_+ - g_0 g_+)[4Em_n q^2+(m_\tau^2-q^2)(m_{\Lambda_c}^2-m_n^2-q^2)], \tag{B8}$$

$$\begin{aligned}\mathcal{A}_{T_L-V_L}=&-\frac{2m_\tau}{q^2}\{[m_{\Lambda_c}^2(m_\tau^2-q^2)-m_\tau^2(m_n^2+q^2)+q^2(4Em_n+m_n^2+q^2)][(m_{\Lambda_c}-m_n)\\&\times(f_0 h_+ + 2f_\perp \tilde{h}_\perp)+(m_{\Lambda_c}+m_n)(g_0\tilde{h}_+ + 2g_\perp h_\perp)]-(m_\tau^2-q^2)[(m_{\Lambda_c}+m_n)\\&\times s_-(f_+ h_+ + 2f_\perp h_\perp)+(m_{\Lambda_c}-m_n)s_+(g_+\tilde{h}_+ + 2g_\perp\tilde{h}_\perp)]\},\end{aligned} \tag{B9}$$

$$\begin{aligned}\mathcal{A}_{T_L-V_R}=&-\frac{2m_\tau}{q^2}\{[m_{\Lambda_c}^2(m_\tau^2-q^2)-m_\tau^2(m_n^2+q^2)+q^2(4Em_n+m_n^2+q^2)][(m_{\Lambda_c}-m_n)\\&\times(f_0 h_+ + 2f_\perp \tilde{h}_\perp)-(m_{\Lambda_c}+m_n)(g_0\tilde{h}_+ + 2g_\perp h_\perp)]-(m_\tau^2-q^2)[(m_{\Lambda_c}+m_n)\\&\times s_-(f_+ h_+ + 2f_\perp h_\perp)-(m_{\Lambda_c}-m_n)s_+(g_+\tilde{h}_+ + 2g_\perp\tilde{h}_\perp)]\},\end{aligned} \tag{B10}$$

$$\mathcal{A}_{T_L-S_L}=\frac{2}{m_c}[4Em_n q^2+(m_\tau^2-q^2)(m_{\Lambda_c}^2-m_p^2-q^2)]\Big[f_0 h_+(m_{\Lambda_c}-m_p)+g_0\tilde{h}_+(m_{\Lambda_c}+m_n)\Big], \tag{B11}$$

$$\mathcal{A}_{T_L-S_R}=\frac{2}{m_c}[4Em_n q^2+(m_\tau^2-q^2)(m_{\Lambda_c}^2-m_n^2-q^2)]\Big[f_0 h_+(m_{\Lambda_c}-m_p)-g_0\tilde{h}_+(m_{\Lambda_c}+m_p)\Big], \tag{B12}$$

$$\mathcal{A}_{S_L-S_R}=\frac{m_\tau^2-q^2}{2m_c^2}\Big[f_0^2(m_{\Lambda_c}-m_n)^2 s_+ - g_0^2(m_{\Lambda_c}+m_n)^2 s_-\Big]. \tag{B13}$$

APPENDIX C: DETAILS OF THE POLARIZATION VECTORS OF τ AND Λ_c

We now present the explicit expressions of $P_L^{l,h}$, $P_P^{l,h}$, and $P_T^{l,h}$ of the outgoing τ and Λ_c. These components of the polarization vectors are defined in Eq. (20) and read

$$\begin{aligned}P_a^{l,h}&=-(\mathcal{P}\cdot N_a)^{l,h}\\&=\frac{\mathrm{Tr}[\rho_{l,h}\gamma_5 \not{N}_a]}{\mathrm{Tr}[\rho_{l,h}]}=\frac{\mathcal{A}_a^{(l,h)}}{2m_{(\tau,\Lambda_c)}|\mathcal{M}|^2}.\end{aligned} \tag{C1}$$

Note that the trace over the spin density matrices $\rho_{l,h}$ has been replaced in the last step by

$$\mathrm{Tr}[\rho_{l,h}]=2m_{(\tau,\Lambda_c)}|\mathcal{M}|^2, \tag{C2}$$

which can be inferred from Eqs. (13) and (15), and the amplitude squared $|\mathcal{M}|^2$ has been given in Eq. (B1). In addition, the trace in the numerator has been redefined as $\mathcal{A}_a^{(l,h)}$, which are given, respectively, by

$$\begin{aligned}\mathcal{A}_a^l=&|1+g_V^{LL}|^2\mathcal{A}_{V_L-V_L}^l+|g_V^R|^2\mathcal{A}_{V_R-V_R}^l+(|g_S^L|^2+|g_S^R|^2)\mathcal{A}_{S_L-S_L}^l\\&+|g_T^L|^2\mathcal{A}_{T_L-T_L}^l+2\mathrm{Re}[g_V^R(1+g_V^{L*})\mathcal{A}_{V_R-V_L}^l+2\mathrm{Re}[g_T^L(1+g_V^{L*})\mathcal{A}_{T_L-V_L}^l]\\&+2\mathrm{Re}[(g_S^L(1+g_V^{L*})+g_S^R g_V^{R*})\mathcal{A}_{S_L-V_L}^l]+2\mathrm{Re}[g_S^L g_S^{R*}\mathcal{A}_{S_L-S_R}^l]\\&+2\mathrm{Re}[(g_S^R(1+g_V^{L*})+g_S^L g_V^{R*})\mathcal{A}_{S_R-V_L}^l]+2\mathrm{Re}[g_T^L g_V^{R*}\mathcal{A}_{T_L-V_R}^l]\\&+2\mathrm{Re}[g_T^L g_S^{L*}\mathcal{A}_{T_L-S_L}^l]+2\mathrm{Re}[g_T^L g_S^{R*}\mathcal{A}_{T_L-S_R}^l],\end{aligned} \tag{C3}$$

$$\begin{aligned}\mathcal{A}_a^h = {} & |1+g_V^{LL}|^2\mathcal{A}^h_{V_L-V_L} + |g_V^R|^2\mathcal{A}^h_{V_R-V_R} + (|g_S^L|^2-|g_S^R|^2)\mathcal{A}^h_{S_L-S_L} \\ & + |g_T^L|^2\mathcal{A}^h_{T_L-T_L} + 2\mathrm{Re}[g_V^R(1+g_V^{L*})\mathcal{A}^h_{V_R-V_L}] + 2\mathrm{Re}[g_T^L(1+g_V^{L*})\mathcal{A}^h_{T_L-V_L}] \\ & + 2\mathrm{Re}[g_S^L(1+g_V^{L*})\mathcal{A}^h_{S_L-V_L}] + 2\mathrm{Re}[g_S^R(1+g_V^{L*})\mathcal{A}^h_{S_R-V_L}] \\ & + 2\mathrm{Re}[g_S^R g_V^{R*}\mathcal{A}^h_{S_R-V_R}] + 2\mathrm{Re}[g_S^L g_V^{R*}\mathcal{A}^h_{S_L-V_R}] + 2\mathrm{Re}[g_T^L g_V^{R*}\mathcal{A}^h_{T_L-V_R}] \\ & + 2\mathrm{Re}[g_T^L g_S^{L*}\mathcal{A}^h_{T_L-S_L}] + 2\mathrm{Re}[g_T^L g_S^{R*}\mathcal{A}^h_{T_L-S_R}] + 2\mathrm{Re}[g_S^L g_S^{R*}\mathcal{A}^h_{S_L-S_R}]. \end{aligned} \tag{C4}$$

The explicit expressions of all the $\mathcal{A}^{l,h}$ on the right-hand side of Eqs. (C3) and (C4) are presented as follows:

$$\begin{aligned}\mathcal{A}^l_{V_L-V_L} = {} & \frac{2m_\tau^4(N_a\cdot k)}{q^4}[f_0^2(m_{\Lambda_c}-m_n)^2 s_+ + g_0^2(m_{\Lambda_c}+m_n)^2 s_-] - \frac{2m_\tau^2(m_{\Lambda_c}^2-m_n^2)}{q^4} \\ & \times (f_0 f_+ + g_0 g_+)\{(N_a\cdot k)[4Em_n q^2 + (m_\tau^2-q^2)(2m_{\Lambda_c}^2-2m_n^2-q^2)] \\ & -q^2(m_\tau^2-q^2)(N_a\cdot p + N_a\cdot p')\} + 2m_\tau^2\left[\frac{f_+^2(m_{\Lambda_c}+m_n)^2}{q^4 s_+} + \frac{g_+^2(m_{\Lambda_c}-m_n)^2}{q^4 s_-}\right] \\ & \times\Big\{(N_a\cdot k)\Big[(m_{\Lambda_c}^2-m_n^2)\Big(m_\tau^2(m_{\Lambda_c}^2-m_n^2-q^2) - q^2(2m_{\Lambda_c}^2-4m_nE-2m_n^2+q^2)\Big) \\ & +q^4(4m_{\Lambda_c}^2-q^2)\Big] - q^2(N_a\cdot p + N_a\cdot p')[4Em_n q^2 + (m_\tau^2-q^2)(m_{\Lambda_c}^2-m_n^2-q^2)]\Big\} \\ & - 8m_\tau^2 f_\perp g_\perp[(N_a\cdot p)(m_\tau^2-q^2-2Em_n) + 2Em_n(N_a\cdot p')] \\ & + 4m_\tau^2\left(\frac{f_\perp^2}{s_+} + \frac{g_\perp^2}{s_-}\right)\Big\{(N_a\cdot p)[2Em_n(m_{\Lambda_c}^2-m_p^2+q^2) + (m_\tau^2-q^2)(m_{\Lambda_c}^2+m_p^2-q^2)] \\ & + 2m_n(N_a\cdot p')\Big[E(m_n^2-m_{\Lambda_c}^2+q^2) + m_n(q^2-m_\tau^2)\Big]\Big\}, \end{aligned} \tag{C5}$$

$$\begin{aligned}\mathcal{A}^l_{V_R-V_R} = {} & \frac{2m_\tau^4(N_a\cdot k)}{q^4}[f_0^2(m_{\Lambda_c}-m_p)^2 s_+ + g_0^2(m_{\Lambda_c}+m_n)^2 s_-] - \frac{2m_\tau^2(m_{\Lambda_c}^2-m_n^2)}{q^4} \\ & \times (f_0 f_+ + g_0 g_+)\{(N_a\cdot k)[4Em_n q^2 + (m_\tau^2-q^2)(2m_{\Lambda_c}^2-2m_n^2-q^2)] \\ & - q^2(m_\tau^2-q^2)(N_a\cdot p + N_a\cdot p')\} + 2m_\tau^2\left[\frac{f_+^2(m_{\Lambda_c}+m_n)^2}{q^4 s_+} + \frac{g_+^2(m_{\Lambda_c}-m_n)^2}{q^4 s_-}\right] \\ & \times\Big\{(N_a\cdot k)\Big[(m_{\Lambda_c}^2-m_n^2)\Big(m_\tau^2(m_{\Lambda_c}^2-m_n^2-q^2) - q^2(2m_{\Lambda_c}^2-4m_nE-2m_n^2+q^2)\Big) \\ & + q^4(4m_{\Lambda_c}^2-q^2)\Big] - q^2(N_a\cdot p + N_a\cdot p')[4Em_n q^2 + (m_\tau^2-q^2)(m_{\Lambda_c}^2-m_n^2-q^2)]\Big\} \\ & + 8m_\tau^2 f_\perp g_\perp[(N_a\cdot p)(m_\tau^2-q^2-2Em_n) + 2Em_n(N_a\cdot p')] \\ & + 4m_\tau^2\left(\frac{f_\perp^2}{s_+} + \frac{g_\perp^2}{s_-}\right)\{(N_a\cdot p)[2Em_n(m_{\Lambda_c}^2-m_n^2+q^2) + (m_\tau^2-q^2)(m_{\Lambda_c}^2+m_n^2-q^2)] \\ & + 2m_n(N_a\cdot p')[E(m_n^2-m_{\Lambda_c}^2+q^2) + m_n(q^2-m_\tau^2)]\}, \end{aligned} \tag{C6}$$

$$\mathcal{A}^l_{S_L-S_L} = \mathcal{A}_{S_L-S_L}\frac{4m_\tau^2(k\cdot N_a)}{m_\tau^2-q^2}, \tag{C7}$$

$$\mathcal{A}^l_{T_L-T_L} = 32m_\tau^2\left(\frac{h_+^2}{s_+}+\frac{\tilde{h}_+^2}{s_-}\right)\Big\{2(N_a\cdot p)[2Em_n(m_{\Lambda_c}^2-m_n^2+q^2)+(m_\tau^2-q^2)(m_{\Lambda_c}^2+m_n^2-q^2)]$$
$$+4m_n(N_a\cdot p')[E(m_n^2-m_{\Lambda_c}^2+q^2)+m_n(q^2-m_\tau^2)]+(N_i\cdot k)s_+s_-\Big\}$$
$$-32m_\tau^2\Big\{(N_a\cdot k)(m_\tau^2-q^2)s_-s_+-[4Em_nq^2+(m_\tau^2-q^2)(m_{\Lambda_c}^2-m_n^2-q^2)]$$
$$\times[(N_a\cdot p)(m_{\Lambda_c}^2-m_n^2+q^2)+(N_a\cdot p')(m_n^2-m_{\Lambda_c}^2+q^2)]\Big\}\left[\frac{(m_{\Lambda_c}-m_n)^2\tilde{h}_\perp^2}{q^4s_-}\right.$$
$$\left.+\frac{(m_{\Lambda_c}+m_n)^2h_\perp^2}{q^4s_+}\right]-\frac{128m_\tau^2(m_{\Lambda_c}^2-m_n^2)h_\perp\tilde{h}_\perp}{q^4}\Big\{(N_a\cdot p)[2Em_nq^2+(m_{\Lambda_c}^2-m_p^2)(m_\tau^2-q^2)]$$
$$-(N_a\cdot p')[2Em_nq^2+(m_\tau^2-q^2)(m_{\Lambda_c}^2-m_n^2-q^2)]\Big\}, \tag{C8}$$

$$\mathcal{A}^l_{V_R-V_L} = \frac{2m_\tau^4(N_a\cdot k)}{q^4}[f_0^2(m_{\Lambda_c}-m_n)^2s_+-g_0^2(m_{\Lambda_c}+m_n)^2s_-]-\frac{2m_\tau^2(m_{\Lambda_c}^2-m_n^2)}{q^4}$$
$$\times(f_0f_+-g_0g_+)\{(N_a\cdot k)[4Em_nq^2+(m_\tau^2-q^2)(2m_{\Lambda_c}^2-2m_n^2-q^2)]$$
$$-q^2(m_\tau^2-q^2)(N_a\cdot p+N_a\cdot p')\}+2m_\tau^2\left[\frac{f_+^2(m_{\Lambda_c}+m_n)^2}{q^4s_+}-\frac{g_+^2(m_{\Lambda_c}-m_n)^2}{q^4s_-}\right]$$
$$\times\Big\{(N_a\cdot k)[(m_{\Lambda_c}^2-m_n^2)(m_\tau^2(m_{\Lambda_c}^2-m_n^2-q^2)-q^2(2m_{\Lambda_c}^2-4m_nE-2m_n^2+q^2))$$
$$+q^4(4m_{\Lambda_c}^2-q^2)]-q^2(N_a\cdot p+N_a\cdot p')[4Em_nq^2+(m_\tau^2-q^2)(m_{\Lambda_c}^2-m_n^2-q^2)]\Big\}$$
$$+4m_\tau^2\left(\frac{f_\perp^2}{s_+}-\frac{g_\perp^2}{s_-}\right)\Big\{(N_a\cdot p)[2Em_n(m_{\Lambda_c}^2-m_n^2+q^2)+(m_\tau^2-q^2)$$
$$\times(m_{\Lambda_c}^2+m_n^2-q^2)]+2m_n(N_a\cdot p')[E(m_n^2-m_{\Lambda_c}^2+q^2)+m_n(q^2-m_\tau^2)]\Big\}, \tag{C9}$$

$$\mathcal{A}^l_{S_L-V_L} = -\frac{2m_\tau^3(N_a\cdot k)}{m_cq^2}\{f_0^2(m_{\Lambda_c}-m_n)^2s_++g_0^2(m_{\Lambda_c}+m_n)^2s_-\}-\frac{2m_\tau(m_{\Lambda_c}^2-m_n^2)}{m_cq^2}$$
$$\times(f_0f_++g_0g_+)\Big\{q^2(m_\tau^2-q^2)(N_a\cdot p')+(N_a\cdot p-N_a\cdot p')$$
$$\times[2Em_nq^2+(m_{\Lambda_c}^2-m_n^2)(m_\tau^2-q^2)]-2iq^2\varepsilon_{\{k\},\{k'\},\{N_a\},\{p\}}\Big\}, \tag{C10}$$

$$\mathcal{A}^l_{S_R-V_L} = -\frac{2m_\tau^3(N_i\cdot k)}{m_cq^2}\{f_0^2(m_{\Lambda_c}-m_n)^2s_+-g_0^2(m_{\Lambda_c}+m_n)^2s_-\}-\frac{2m_\tau(m_{\Lambda_c}^2-m_n^2)}{m_cq^2}$$
$$\times(f_0f_+-g_0g_+)\Big\{q^2(m_\tau^2-q^2)(N_a\cdot p')+(N_a\cdot p-N_a\cdot p')$$
$$\times[2Em_nq^2+(m_{\Lambda_c}^2-m_p^2)(m_\tau^2-q^2)]-2iq^2\varepsilon_{\{k\},\{k'\},\{N_a\},\{p\}}\Big\}, \tag{C11}$$

$$\mathcal{A}^{l}_{T_L-V_L} = -8m_\tau^3\left[\frac{(m_{\Lambda_c}-m_n)f_0h_+}{q^2}+\frac{(m_{\Lambda_c}+m_n)g_0\tilde{h}_+}{q^2}\right][(N_a\cdot p)(2Em_n-m_\tau^2+q^2)$$
$$-2(Em_n(N_a\cdot p')+i\varepsilon_{\{k\}\{k'\}\{N_a\}\{p\}})]+[4Em_nq^2+(m_\tau^2-q^2)(m_{\Lambda_c}^2-m_n^2-q^2)]$$
$$\times[2i\varepsilon_{\{k\}\{k'\}\{N_a\}\{p\}}+(N_a\cdot p)(m_{\Lambda_c}^2-m_n^2+m_\tau^2-2Em_n)+(N_a\cdot p')(2Em_n-m_{\Lambda_c}^2+m_n^2+q^2)]$$
$$\times\left[\frac{8m_\tau(m_{\Lambda_c}+m_n)f_\perp h_\perp}{s_+q^2}+\frac{8m_\tau(m_{\Lambda_c}-m_n)g_\perp\tilde{h}_\perp}{s_-q^2}\right]+8m_\tau(q^2-m_\tau^2)$$
$$\times\left[\frac{(m_{\Lambda_c}-m_n)f_\perp\tilde{h}_\perp}{q^2}+\frac{(m_{\Lambda_c}+m_n)g_\perp h_\perp}{q^2}\right][2i\varepsilon_{\{k\}\{k'\}\{N_a\}\{p\}}+(N_a\cdot p)(m_{\Lambda_c}^2-m_n^2+m_\tau^2-2Em_n)$$
$$+(N_a\cdot p')(2Em_n-m_{\Lambda_c}^2+m_n^2+q^2)]+8m_\tau\Big\{[4m_n^2q^2(m_\tau^2-2E^2)$$
$$+2Em_n(m_\tau^2-3q^2)(m_n^2-m_{\Lambda_c}^2+q^2)-q^2s_-s_+](N_a\cdot p+N_a\cdot p')-(m_\tau^2+q^2)$$
$$\times[(m_\tau^2-q^2)(m_n^2-m_{\Lambda_c}^2+q^2)-4Em_nq^2](N_a\cdot p)-2i[4Em_nq^2+(m_\tau^2-q^2)$$
$$\times(m_{\Lambda_c}^2-m_n^2-q^2)]\varepsilon_{\{k\}\{k'\}\{N_a\}\{p\}}\Big\}\left[\frac{(m_{\Lambda_c}+m_n)f_+h_+}{s_+q^2}+\frac{(m_{\Lambda_c}-m_n)g_+\tilde{h}_+}{s_-q^2}\right], \tag{C12}$$

$$\mathcal{A}^{l}_{T_L-V_R} = -8m_\tau^3\left[\frac{(m_{\Lambda_c}-m_n)f_0h_+}{q^2}-\frac{(m_{\Lambda_c}+m_n)g_0\tilde{h}_+}{q^2}\right][(N_a\cdot p)(2Em_n-m_\tau^2+q^2)$$
$$-2(Em_n(N_a\cdot p')+i\varepsilon_{\{k\}\{k'\}\{N_a\}\{p\}})]+[4Em_nq^2+(m_\tau^2-q^2)(m_{\Lambda_c}^2-m_n^2-q^2)]$$
$$\times[2i\varepsilon_{\{k\}\{k'\}\{N_a\}\{p\}}+(N_a\cdot p)(m_{\Lambda_c}^2-m_n^2+m_\tau^2-2Em_n)+(N_a\cdot p')(2Em_n-m_{\Lambda_c}^2$$
$$+m_n^2+q^2)]\left[\frac{8m_\tau(m_{\Lambda_c}+m_n)f_\perp h_\perp}{s_+q^2}-\frac{8m_\tau(m_{\Lambda_c}-m_n)g_\perp\tilde{h}_\perp}{s_-q^2}\right]+8m_\tau(q^2-m_\tau^2)$$
$$\times\left[\frac{(m_{\Lambda_c}-m_n)f_\perp\tilde{h}_\perp}{q^2}-\frac{(m_{\Lambda_c}+m_n)g_\perp h_\perp}{q^2}\right][2i\varepsilon_{\{k\}\{k'\}\{N_a\}\{p\}}+(N_a\cdot p)(m_{\Lambda_c}^2-m_n^2$$
$$+m_\tau^2-2Em_n)+(N_a\cdot p')(2Em_n-m_{\Lambda_c}^2+m_n^2+q^2)]+8m_\tau\Big\{[4m_n^2q^2(m_\tau^2-2E^2)$$
$$+2Em_n(m_\tau^2-3q^2)(m_n^2-m_{\Lambda_c}^2+q^2)-q^2s_-s_+](N_a\cdot p+N_a\cdot p')-(m_\tau^2+q^2)$$
$$\times[(m_\tau^2-q^2)(m_n^2-m_{\Lambda_c}^2+q^2)-4Em_nq^2](N_a\cdot p)-2i[4Em_nq^2+(m_\tau^2-q^2)$$
$$\times(m_{\Lambda_c}^2-m_n^2-q^2)]\varepsilon_{\{k\}\{k'\}\{N_a\}\{p\}}\Big\}\left[\frac{(m_{\Lambda_c}+m_n)f_+h_+}{s_+q^2}-\frac{(m_{\Lambda_c}-m_n)g_+\tilde{h}_+}{s_-q^2}\right], \tag{C13}$$

$$\mathcal{A}^{l}_{T_L-S_L} = \frac{8m_\tau^2}{m_c}[2i\varepsilon_{\{k\},\{N_a\},\{p\},\{p'\}}+(N_a\cdot p)(2Em_n-m_\tau^2+q^2)-2Em_n(N_a\cdot p')]$$
$$\times[f_0h_+(m_{\Lambda_c}-m_n)+g_0\tilde{h}_+(m_{\Lambda_c}+m_n)], \tag{C14}$$

$$\mathcal{A}^{l}_{T_L-S_R} = \frac{8m_\tau^2}{m_c}[2i\varepsilon_{\{k\},\{N_a\},\{p\},\{p'\}}+(N_a\cdot p)(2Em_n-m_\tau^2+q^2)-2Em_n(N_a\cdot p')]$$
$$\times[f_0h_+(m_{\Lambda_c}-m_n)-g_0\tilde{h}_+(m_{\Lambda_c}+m_n)], \tag{C15}$$

$$\mathcal{A}^{l}_{S_L-S_R} = \mathcal{A}_{S_L-S_R}\frac{2m_\tau(k\cdot N_a)}{m_\tau^2-q^2}, \tag{C16}$$

$$
\begin{aligned}
\mathcal{A}^h_{V_L-V_L} = & -2m_{\Lambda_c}\{(N_a\cdot k)[4Em_n(m_n^2-m_{\Lambda_c}^2)+(q^2-m_\tau^2)(m_{\Lambda_c}^2+3m_n^2-q^2)+2s_+s_-] \\
& +(N_a\cdot p+N_a\cdot p')[4Em_nq^2+(m_\tau^2-q^2)(m_{\Lambda_c}^2-m_n^2-q^2)]\} \\
& \times\left[\frac{(m_{\Lambda_c}+m_n)f_+f_\perp}{s_+}+\frac{(m_{\Lambda_c}-m_n)g_+g_\perp}{s_-}\right]+\frac{2f_0g_0m_\tau^2(m_{\Lambda_c}^2-m_n^2)}{q^4}(m_\tau^2-q^2) \\
& \times[2m_{\Lambda_c}^2(N_a\cdot p)-(N_a\cdot p')(m_{\Lambda_c}^2+m_n^2-q^2)]+4m_{\Lambda_c}[4Em_nq^2+(m_\tau^2-q^2) \\
& \times(m_{\Lambda_c}^2-m_n^2-q^2)]\{[s_+s_--2Em_n(m_{\Lambda_c}^2-m_n^2+q^2)+(q^2-m_\tau^2)(m_{\Lambda_c}^2+m_n^2-q^2)](N_a\cdot p) \\
& -[s_+s_-+2Em_n(m_n^2-m_{\Lambda_c}^2+q^2)+2m_n^2(q^2-m_\tau^2)](N_a\cdot p')\} \\
& \times\frac{[(m_{\Lambda_c}+m_n)f_+g_\perp+(m_{\Lambda_c}-m_n)f_\perp g_+]}{q^2s_-s_+}+\left[\frac{(m_{\Lambda_c}-m_n)f_0g_\perp}{q^2s_-}+\frac{(m_{\Lambda_c}+m_n)f_\perp g_0}{q^2s_+}\right] \\
& \times 4m_{\Lambda_c}m_\tau^2\{(N_a\cdot p)[2Em_n(m_{\Lambda_c}^2-m_n^2+q^2)+(m_\tau^2-q^2)(m_{\Lambda_c}^2+m_n^2-q^2)] \\
& +2m_n(N_a\cdot p')[E(m_n^2-m_{\Lambda_c}^2+q^2)+m_n(q^2-m_\tau^2)]+(N_a\cdot k)s_+s_-\}+2\left(\frac{f_\perp^2}{s_+}+\frac{g_\perp^2}{s_-}\right) \\
& \times[4Em_nq^2+(m_\tau^2-q^2)(m_{\Lambda_c}^2-m_n^2-q^2)][2m_{\Lambda_c}^2(N_a\cdot p)-(N_a\cdot p')(m_{\Lambda_c}^2+m_n^2-q^2)] \\
& +\frac{4f_\perp g_\perp}{s_-s_+}\{8E^2m_n^2q^2+(m_\tau^2-q^2)[2m_{\Lambda_c}^2(m_n^2+q^2)-4Em_n(m_p^2-m_{\Lambda_c}^2+q^2) \\
& -m_n^4+2m_n^2m_\tau^2-q^4]\}[2m_{\Lambda_c}^2(N_a\cdot p)-(N_a\cdot p')(m_{\Lambda_c}^2+m_n^2-q^2)] \\
& -2m_\tau^2\{[4Em_nq^2+(m_\tau^2-q^2)(m_{\Lambda_c}^2-m_n^2-q^2)][2m_{\Lambda_c}^2(N_a\cdot p)-(N_a\cdot p') \\
& \times(m_{\Lambda_c}^2+m_n^2-q^2)]\}\left[\frac{f_0g_+(m_{\Lambda_c}-m_n)^2}{q^4s_-}+\frac{f_+g_0(m_{\Lambda_c}+m_n)^2}{q^4s_+}\right]-\frac{2(m_{\Lambda_c}^2-m_n^2)f_+g_+}{q^4s_-s_+} \\
& \times\left\{16E^2m_n^2q^4+(m_\tau^2-q^2)\left[m_\tau^2(m_n^2-m_{\Lambda_c}^2+q^2)^2-4m_nq^2(2E(m_n^2-m_{\Lambda_c}^2+q^2)+m_nq^2)\right]\right\} \\
& \times[2m_{\Lambda_c}^2(N_a\cdot p)-(N_a\cdot p')(m_{\Lambda_c}^2+m_n^2-q^2)],
\end{aligned}
\tag{C17}
$$

$$
\begin{aligned}
\mathcal{A}^h_{V_R-V_R} = & -2m_{\Lambda_c}\{(N_a\cdot k)[4Em_n(m_n^2-m_{\Lambda_c}^2)+(q^2-m_\tau^2)(m_{\Lambda_c}^2+3m_n^2-q^2)+2s_+s_-] \\
& +(N_a\cdot p+N_a\cdot p')[4Em_nq^2+(m_\tau^2-q^2)(m_{\Lambda_c}^2-m_n^2-q^2)]\} \\
& \times\left[\frac{(m_{\Lambda_c}+m_n)f_+f_\perp}{s_+}+\frac{(m_{\Lambda_c}-m_n)g_+g_\perp}{s_-}\right]+\frac{2f_0g_0m_\tau^2(m_{\Lambda_c}^2-m_n^2)}{q^4}(m_\tau^2-q^2) \\
& \times[2m_{\Lambda_c}^2(N_a\cdot p)-(N_a\cdot p')(m_{\Lambda_c}^2+m_n^2-q^2)]+4m_{\Lambda_c}[4Em_nq^2+(m_\tau^2-q^2) \\
& \times(m_{\Lambda_c}^2-m_n^2-q^2)]\{[s_+s_--2Em_n(m_{\Lambda_c}^2-m_n^2+q^2)+(q^2-m_\tau^2)(m_{\Lambda_c}^2+m_n^2-q^2)](N_a\cdot p) \\
& -[s_+s_-+2Em_n(m_n^2-m_{\Lambda_c}^2+q^2)+2m_n^2(q^2-m_\tau^2)](N_a\cdot p')\} \\
& \times\frac{[(m_{\Lambda_c}+m_n)f_+g_\perp+(m_{\Lambda_c}-m_n)f_\perp g_+]}{q^2s_-s_+}+\left[\frac{(m_{\Lambda_c}-m_n)f_0g_\perp}{q^2s_-}+\frac{(m_{\Lambda_c}+m_n)f_\perp g_0}{q^2s_+}\right] \\
& \times 4m_{\Lambda_c}m_\tau^2\{(N_a\cdot p)[2Em_n(m_{\Lambda_c}^2-m_n^2+q^2)+(m_\tau^2-q^2)(m_{\Lambda_c}^2+m_n^2-q^2)] \\
& +2m_n(N_a\cdot p')[E(m_n^2-m_{\Lambda_c}^2+q^2)+m_n(q^2-m_\tau^2)]+(N_a\cdot k)s_+s_-\}+2\left(\frac{f_\perp^2}{s_+}+\frac{g_\perp^2}{s_-}\right) \\
& \times[4Em_nq^2+(m_\tau^2-q^2)(m_{\Lambda_c}^2-m_n^2-q^2)][2m_{\Lambda_c}^2(N_a\cdot p)-(N_a\cdot p')(m_{\Lambda_c}^2+m_p^2-q^2)] \\
& -\frac{4f_\perp g_\perp}{s_-s_+}\{8E^2m_n^2q^2+(m_\tau^2-q^2)[2m_{\Lambda_c}^2(m_n^2+q^2)-4Em_n(m_n^2-m_{\Lambda_c}^2+q^2) \\
& -m_n^4+2m_n^2m_\tau^2-q^4]\}[2m_{\Lambda_c}^2(N_a\cdot p)-(N_a\cdot p')(m_{\Lambda_c}^2+m_n^2-q^2)]
\end{aligned}
$$

$$
\begin{aligned}
&- 2m_\tau^2\{[4Em_nq^2 + (m_\tau^2 - q^2)(m_{\Lambda_c}^2 - m_n^2 - q^2)][2m_{\Lambda_c}^2(N_a\cdot p) - (N_a\cdot p')\\
&\times (m_{\Lambda_c}^2 + m_n^2 - q^2)]\}\left[\frac{f_0 g_+(m_{\Lambda_c} - m_n)^2}{q^4 s_-} + \frac{f_+ g_0(m_{\Lambda_c} + m_n)^2}{q^4 s_+}\right] + \frac{2(m_{\Lambda_c}^2 - m_n^2) f_+ g_+}{q^4 s_- s_+}\\
&\times \{16E^2 m_n^2 q^4 + (m_\tau^2 - q^2)[m_\tau^2(m_n^2 - m_{\Lambda_c}^2 + q^2)^2 - 4m_n q^2(2E(m_n^2 - m_{\Lambda_c}^2 + q^2)\\
&+ m_n q^2)]\}[2m_{\Lambda_c}^2(N_a\cdot p) - (N_a\cdot p')(m_{\Lambda_c}^2 + m_n^2 - q^2)],
\end{aligned}
\tag{C18}
$$

$$
\mathcal{A}^h_{S_L - S_L} = \frac{2f_0 g_0(m_{\Lambda_c}^2 - m_n^2)(m_\tau^2 - q^2)}{m_c^2}[2m_{\Lambda_c}^2(N_a\cdot p) - (N_a\cdot p')(m_{\Lambda_c}^2 + m_n^2 - q^2)],
\tag{C19}
$$

$$
\begin{aligned}
\mathcal{A}^h_{T_L - T_L} &= 32m_\tau^2\left[\frac{\tilde{h}_\perp^2(m_{\Lambda_c} - m_n)^2}{s_- q^4} + \frac{h_\perp^2(m_{\Lambda_c} + m_n)^2}{s_+ q^4}\right][(m_\tau^2 - q^2)(m_{\Lambda_c}^2 - m_n^2 - q^2) + 4Em_nq^2]\\
&\times [2m_{\Lambda_c}^2(N_a\cdot p) - (N_a\cdot p')(m_{\Lambda_c}^2 + m_n^2 - q^2)] - 64m_{\Lambda_c}[(m_\tau^2 - q^2)(m_{\Lambda_c}^2 - m_n^2 - q^2)\\
&+ 4Em_nq^2]\{[s_- s_+ - 2Em_n(m_{\Lambda_c}^2 - m_n^2 + q^2) + (q^2 - m_\tau^2)(m_{\Lambda_c}^2 + m_n^2 - q^2)](N_a\cdot p)\\
&- [s_- s_+ + 2m_n E_{\nu_\tau}(m_n^2 - m_{\Lambda_c}^2 + q^2) + 2m_n^2(q^2 - m_\tau^2)](N_a\cdot p')\}\\
&\times \frac{h_+\tilde{h}_\perp(m_{\Lambda_c} - m_n) + \tilde{h}_+ h_\perp(m_{\Lambda_c} + m_n)}{s_- s_+ q^2} + \left[\frac{h_+ h_\perp(m_{\Lambda_c} + m_n)}{s_+ q^2} + \frac{\tilde{h}_+\tilde{h}_\perp(m_{\Lambda_c} - m_n)}{s_- q^2}\right]\\
&\times 64m_{\Lambda_c}m_\tau^2\{[s_- s_+ - 2Em_n(m_{\Lambda_c}^2 - m_n^2 + q^2) + (q^2 - m_\tau^2)(m_{\Lambda_c}^2 + m_n^2 - q^2)](N_a\cdot p)\\
&- [s_- s_+ + 2m_n E(m_n^2 - m_{\Lambda_c}^2 + q^2) + 2m_n^2(q^2 - m_\tau^2)](N_a\cdot p')\}\\
&- \frac{64h_\perp\tilde{h}_\perp(m_{\Lambda_c}^2 - m_n^2)}{s_- s_+ q^4}\{(m_\tau^2 - q^2)[m_\tau^2(s_- s_+ + 2m_n^2 q^2) - 4m_n q^2 E(m_n^2\\
&- m_{\Lambda_c}^2 + q^2) - 2m_n^2 q^4] + 8E^2 m_n^2 q^4\}[2m_{\Lambda_c}^2(N_a\cdot p) - (N_a\cdot p')(m_{\Lambda_c}^2 + m_n^2 - q^2)]\\
&- \frac{32h_+\tilde{h}_+}{s_- s_+}\{(m_\tau^2 - q^2)[-4m_n^2(q^2 - m_\tau^2) - 8m_n E(m_n^2 - m_{\Lambda_c}^2 + q^2) - s_- s_+] + 16E^2 m_n^2 q^2\}\\
&\times [2m_{\Lambda_c}^2(N_a\cdot p) - (N_a\cdot p')(m_{\Lambda_c}^2 + m_n^2 - q^2)],
\end{aligned}
\tag{C20}
$$

$$
\begin{aligned}
\mathcal{A}^h_{V_R - V_L} &= 8im_{\Lambda_c}[f_+ g_\perp(m_{\Lambda_c} + m_n) - f_\perp g_+(m_{\Lambda_c} - m_n)]\varepsilon_{\{k\}\{k'\}\{N_a\}\{p\}} + 2[4Em_nq^2\\
&+ (m_\tau^2 - q^2)(m_{\Lambda_c}^2 - m_n^2 - q^2)][2m_{\Lambda_c}^2(N_a\cdot p) - (N_a\cdot p')(m_{\Lambda_c}^2 + m_n^2 - q^2)]\left(\frac{f_\perp^2}{s_+} - \frac{g_\perp^2}{s_-}\right)\\
&- 2m_{\Lambda_c}\{[2s_+ s_- + 4Em_n(m_n^2 - m_{\Lambda_c}^2) + (q^2 - m_\tau^2)(m_{\Lambda_c}^2 + 3m_n^2 - q^2)](N_a\cdot k)\\
&+ [4Em_nq^2 + (m_\tau^2 - q^2)(m_{\Lambda_c}^2 - m_n^2 - q^2)]\}(N_a\cdot p + N_a\cdot p')\\
&\times \left[\frac{f_+ f_\perp(m_{\Lambda_c} + m_n)}{s_+} - \frac{g_+ g_\perp(m_{\Lambda_c} - m_n)}{s_-}\right],
\end{aligned}
\tag{C21}
$$

$$
\begin{aligned}
\mathcal{A}^h_{S_L - V_L} &= -\frac{4im_{\Lambda_c}m_\tau\varepsilon_{\{k\}\{N_a\}\{p\}\{p'\}}}{m_c}[(m_{\Lambda_c} + m_n)g_0 g_\perp + (m_{\Lambda_c} - m_n)f_0 f_\perp]\\
&- \frac{2m_{\Lambda_c}m_\tau}{m_c}\left\{\frac{(m_{\Lambda_c} + m_p)f_\perp g_0}{s_+} + \frac{(m_{\Lambda_c} - m_n)f_0 g_\perp}{s_-}\right\}\{(N_a\cdot p)[2Em_n(m_{\Lambda_c}^2 - m_n^2 + q^2)\\
&+ (m_\tau^2 - q^2)(m_{\Lambda_c}^2 + m_n^2 - q^2)] + 2m_n(N_a\cdot p')[E(m_n^2 - m_{\Lambda_c}^2 + q^2) + m_n(q^2 - m_\tau^2)]\\
&+ (N_a\cdot k)s_+ s_-\} + m_\tau[4Em_nq^2 + (m_\tau^2 - q^2)(m_{\Lambda_c}^2 - m_n^2 - q^2)][2m_{\Lambda_c}^2(N_a\cdot p)\\
&- (N_a\cdot p')(m_{\Lambda_c}^2 + m_n^2 - q^2)]\left[\frac{(m_{\Lambda_c} + m_n)^2 f_+ g_0}{m_c q^2 s_+} + \frac{(m_{\Lambda_c} - m_n)^2 f_0 g_+}{m_c q^2 s_-}\right]\\
&+ \frac{2f_0 g_0 m_\tau(m_{\Lambda_c}^2 - m_n^2)}{m_c q^2}(q^2 - m_\tau^2)[2m_{\Lambda_c}^2(N_a\cdot p) - (N_a\cdot p')(m_{\Lambda_c}^2 + m_n^2 - q^2)],
\end{aligned}
\tag{C22}
$$

$$\mathcal{A}^h_{S_R-V_L} = \frac{4im_{\Lambda_c}m_\tau\varepsilon_{\{k\}\{N_a\}\{p\}\{p'\}}}{m_c}[(m_{\Lambda_c}+m_n)g_0g_\perp-(m_{\Lambda_c}-m_n)f_0f_\perp]$$
$$-\frac{2m_{\Lambda_c}m_\tau}{m_c}\left\{\frac{(m_{\Lambda_c}-m_n)f_0g_\perp}{s_-}-\frac{(m_{\Lambda_c}+m_n)f_\perp g_0}{s_+}\right\}\{(N_a\cdot p)[2Em_n(m^2_{\Lambda_c}-m_p^2+q^2)$$
$$+(m_\tau^2-q^2)(m^2_{\Lambda_c}+m_n^2-q^2)]+2m_n(N_a\cdot p')[E(m_n^2-m^2_{\Lambda_c}+q^2)+m_n(q^2-m_\tau^2)]$$
$$+(N_a\cdot k)s_+s_-\}+m_\tau[4Em_nq^2+(m_\tau^2-q^2)(m^2_{\Lambda_c}-m_n^2-q^2)][2m^2_{\Lambda_c}(N_a\cdot p)$$
$$-(N_a\cdot p')(m^2_{\Lambda_c}+m_n^2-q^2)]\left[\frac{(m_{\Lambda_c}-m_n)^2f_0g_+}{m_cq^2s_-}-\frac{(m_{\Lambda_c}+m_n)^2f_+g_0}{m_cq^2s_+}\right], \tag{C23}$$

$$\mathcal{A}^h_{S_L-V_R} = \frac{4im_{\Lambda_c}m_\tau\varepsilon_{\{k\}\{N_a\}\{p\}\{p'\}}}{m_c}[(m_{\Lambda_c}+m_n)g_0g_\perp-(m_{\Lambda_c}-m_n)f_0f_\perp]$$
$$+\frac{2m_{\Lambda_c}m_\tau}{m_c}\left\{\frac{(m_{\Lambda_c}-m_n)f_0g_\perp}{s_-}-\frac{(m_{\Lambda_c}+m_n)f_\perp g_0}{s_+}\right\}\{(N_a\cdot p)[2Em_n(m^2_{\Lambda_c}-m_n^2+q^2)$$
$$+(m_\tau^2-q^2)(m^2_{\Lambda_c}+m_n^2-q^2)]+2m_n(N_a\cdot p')[E(m_n^2-m^2_{\Lambda_c}+q^2)+m_n(q^2-m_\tau^2)]$$
$$+(N_a\cdot k)s_+s_-\}-m_\tau[4Em_nq^2+(m_\tau^2-q^2)(m^2_{\Lambda_c}-m_n^2-q^2)][2m^2_{\Lambda_c}(N_a\cdot p)$$
$$-(N_a\cdot p')(m^2_{\Lambda_c}+m_n^2-q^2)]\left[\frac{(m_{\Lambda_c}-m_n)^2f_0g_+}{m_cq^2s_-}-\frac{(m_{\Lambda_c}+m_n)^2f_+g_0}{m_cq^2s_+}\right], \tag{C24}$$

$$\mathcal{A}^h_{S_R-V_R} = \frac{4im_{\Lambda_c}m_\tau\varepsilon_{\{k\}\{N_a\}\{p\}\{p'\}}}{m_c}[(m_{\Lambda_c}+m_n)g_0g_\perp+(m_{\Lambda_c}-m_n)f_0f_\perp]$$
$$+\frac{2m_{\Lambda_c}m_\tau}{m_c}\left\{\frac{(m_{\Lambda_c}-m_n)f_0g_\perp}{s_-}+\frac{(m_{\Lambda_c}+m_n)f_\perp g_0}{s_+}\right\}\{(N_a\cdot p)[2Em_n(m^2_{\Lambda_c}-m_n^2+q^2)$$
$$+(m_\tau^2-q^2)(m^2_{\Lambda_c}+m_n^2-q^2)]+2m_n(N_a\cdot p')[E(m_n^2-m^2_{\Lambda_c}+q^2)+m_n(q^2-m_\tau^2)]$$
$$+(N_a\cdot k)s_+s_-\}-m_\tau[4Em_nq^2+(m_\tau^2-q^2)(m^2_{\Lambda_c}-m_n^2-q^2)][2m^2_{\Lambda_c}(N_a\cdot p)$$
$$-(N_a\cdot p')(m^2_{\Lambda_c}+m_n^2-q^2)]\left[\frac{(m_{\Lambda_c}-m_n)^2f_0g_+}{m_cq^2s_-}+\frac{(m_{\Lambda_c}+m_n)^2f_+g_0}{m_cq^2s_+}\right]$$
$$-\frac{2f_0g_0m_\tau(m^2_{\Lambda_c}-m_n^2)}{m_cq^2}(q^2-m_\tau^2)[2m^2_{\Lambda_c}(N_a\cdot p)-(N_a\cdot p')(m^2_{\Lambda_c}+m_n^2-q^2)], \tag{C25}$$

$$\mathcal{A}^h_{T_L-V_L} = 16im_{\Lambda_c}m_\tau\left[\frac{(m^2_{\Lambda_c}-m_n^2)(f_0h_\perp+g_0\tilde{h}_\perp+f_+\tilde{h}_\perp+g_+h_\perp)}{q^2}+f_\perp\tilde{h}_++g_\perp h_+\right]\varepsilon_{\{k\}\{k'\}\{N_a\}\{p\}}$$
$$+8m_{\Lambda_c}m_\tau\left[\frac{g_+\tilde{h}_\perp(m_{\Lambda_c}-m_n)^2}{s_-q^2}+\frac{f_+h_\perp(m_{\Lambda_c}+m_n)^2}{s_+q^2}\right]\{[s_-s_+-2Em_n(m^2_{\Lambda_c}-m_n^2+q^2)$$
$$+(q^2-m_\tau^2)(m^2_{\Lambda_c}+m_n^2-q^2)](N_a\cdot p)-[s_-s_+-2Em_n(m_n^2-m^2_{\Lambda_c}+q^2)$$
$$+2m_n^2(q^2-m_\tau^2)](N_a\cdot p')\}-\left(\frac{g_\perp\tilde{h}_+}{s_-}+\frac{f_\perp h_+}{s_+}\right)$$
$$\times 8m_{\Lambda_c}m_\tau\Big\{s_-s_+(N_a\cdot k)+(N_a\cdot p)[2Em_n(m^2_{\Lambda_c}-m_n^2+q^2)+(m_\tau^2-q^2)(m^2_{\Lambda_c}$$
$$+m_n^2-q^2)]+2m_n(N_a\cdot p')[E(m_n^2-m^2_{\Lambda_c}+q^2)+m_n(q^2-m_\tau^2)]\Big\}$$
$$+4m_\tau\left[\frac{(m_{\Lambda_c}-m_n)(2g_\perp\tilde{h}_\perp-f_0\tilde{h}_+)}{s_-q^2}+\frac{(m_{\Lambda_c}+m_p)(2f_\perp h_\perp-g_0h_+)}{s_+q^2}\right][4Em_nq^2$$

$$+(m_\tau^2-q^2)(m_{\Lambda_c}^2-m_n^2-q^2)][2m_{\Lambda_c}^2(N_a\cdot p)-(N_a\cdot p')(m_{\Lambda_c}^2+m_n^2-q^2)]$$
$$-4m_\tau\left[\frac{(m_{\Lambda_c}+m_n)(2g_\perp h_\perp-f_+\tilde{h}_+)}{q^2}+\frac{(m_{\Lambda_c}-m_n)(2f_\perp\tilde{h}_\perp-g_+h_+)}{q^2}\right](m_\tau^2-q^2)$$
$$\times[2m_{\Lambda_c}^2(N_a\cdot p)-(N_a\cdot p')(m_{\Lambda_c}^2+m_n^2-q^2)]+4m_{\Lambda_c}m_\tau\Big\{(m_\tau^2+q^2)s_-s_+(N_a\cdot k)$$
$$+[4Em_nq^2+(m_\tau^2-q^2)(m_{\Lambda_c}^2-m_n^2-q^2)][(N_a\cdot p)(m_{\Lambda_c}^2-m_n^2+q^2)$$
$$+(N_a\cdot p')(m_n^2-m_{\Lambda_c}^2+q^2)]\Big\}\left[\frac{f_0\tilde{h}_\perp(m_{\Lambda_c}-m_n)^2}{s_-q^4}+\frac{g_0h_\perp(m_{\Lambda_c}+m_n)^2}{s_+q^4}\right], \tag{C26}$$

$$\mathcal{A}^h_{T_L-V_R}=16im_{\Lambda_c}m_\tau\left[\frac{(m_{\Lambda_c}^2-m_n^2)(f_0h_\perp-g_0\tilde{h}_\perp+f_+\tilde{h}_\perp-g_+h_\perp)}{q^2}+f_\perp\tilde{h}_+-g_\perp h_+\right]\varepsilon_{\{k\}\{k'\}\{N_a\}\{p\}}$$
$$+8m_{\Lambda_c}m_\tau\left[\frac{f_+h_\perp(m_{\Lambda_c}+m_n)^2}{s_+q^2}-\frac{g_+\tilde{h}_\perp(m_{\Lambda_c}-m_n)^2}{s_-q^2}\right]\{[s_-s_+-2Em_n(m_{\Lambda_c}^2-m_n^2+q^2)$$
$$+(q^2-m_\tau^2)(m_{\Lambda_c}^2+m_n^2-q^2)](N_a\cdot p)-[s_-s_++2Em_n(m_n^2-m_{\Lambda_c}^2+q^2)$$
$$+2m_n^2(q^2-m_\tau^2)](N_a\cdot p')\}-\left(\frac{f_\perp h_+}{s_+}-\frac{g_\perp\tilde{h}_+}{s_-}\right)8m_{\Lambda_c}m_\tau\{s_-s_+(N_a\cdot k)+(N_a\cdot p)[2Em_n(m_{\Lambda_c}^2-m_n^2+q^2)$$
$$+(m_\tau^2-q^2)(m_{\Lambda_c}^2+m_n^2-q^2)]+2m_n(N_a\cdot p')[E(m_n^2-m_{\Lambda_c}^2+q^2)+m_n(q^2-m_\tau^2)]\}$$
$$+4m_\tau\left[\frac{(m_{\Lambda_c}+m_n)(2f_\perp h_\perp+g_0h_+)}{s_+q^2}-\frac{(m_{\Lambda_c}-m_n)(2g_\perp\tilde{h}_\perp+f_0\tilde{h}_+)}{s_-q^2}\right][4Em_nq^2$$
$$+(m_\tau^2-q^2)(m_{\Lambda_c}^2-m_n^2-q^2)][2m_{\Lambda_c}^2(N_a\cdot p)-(N_a\cdot p')(m_{\Lambda_c}^2+m_n^2-q^2)]$$
$$-4m_\tau\left[\frac{(m_{\Lambda_c}-m_n)(2f_\perp\tilde{h}_\perp+g_+h_+)}{q^2}-\frac{(m_{\Lambda_c}+m_n)(2g_\perp h_\perp+f_+\tilde{h}_+)}{q^2}\right](m_\tau^2-q^2)$$
$$\times[2m_{\Lambda_c}^2(N_a\cdot p)-(N_a\cdot p')(m_{\Lambda_c}^2+m_n^2-q^2)]+4m_{\Lambda_c}m_\tau\{(m_\tau^2+q^2)s_-s_+(N_a\cdot k)$$
$$+[4Em_nq^2+(m_\tau^2-q^2)(m_{\Lambda_c}^2-m_n^2-q^2)][(N_a\cdot p)(m_{\Lambda_c}^2-m_n^2+q^2)$$
$$+(N_a\cdot p')(m_p^2-m_{\Lambda_c}^2+q^2)]\}\left[\frac{f_0\tilde{h}_\perp(m_{\Lambda_c}-m_n)^2}{s_-q^4}-\frac{g_0h_\perp(m_{\Lambda_c}+m_n)^2}{s_+q^4}\right], \tag{C27}$$

$$\mathcal{A}^h_{T_L-S_L}=4[4Em_nq^2+(m_\tau^2-q^2)(m_{\Lambda_c}^2-m_n^2-q^2)][2m_{\Lambda_c}^2(N_a\cdot p)-(N_a\cdot p')(m_{\Lambda_c}^2+m_n^2-q^2)]$$
$$\times\left[\frac{(m_{\Lambda_c}-m_n)f_0\tilde{h}_+}{m_cs_-}+\frac{(m_{\Lambda_c}+m_n)g_0h_+}{m_cs_+}\right]-\frac{16im_{\Lambda_c}(m_{\Lambda_c}^2-m_n^2)\varepsilon_{\{k\}\{k'\}\{N_a\}\{p\}}}{m_c}$$
$$\times(f_0h_\perp+g_0\tilde{h}_\perp)-4\{[4Em_nq^2+(m_\tau^2-q^2)(m_{\Lambda_c}^2-m_n^2-q^2)][(N_a\cdot p)(m_{\Lambda_c}^2-m_n^2+q^2)$$
$$+(N_a\cdot p')(m_n^2-m_{\Lambda_c}^2+q^2)]+(N_a\cdot k)(m_\tau^2+q^2)[m_{\Lambda_c}^4-2m_{\Lambda_c}^2(m_n^2+q^2)$$
$$+(m_n^2-q^2)^2]\}\left[\frac{m_{\Lambda_c}(m_{\Lambda_c}-m_n)^2f_0\tilde{h}_\perp}{m_cq^2s_-}+\frac{m_{\Lambda_c}(m_{\Lambda_c}+m_n)^2g_0h_\perp}{m_cq^2s_+}\right], \tag{C28}$$

$$\mathcal{A}^h_{T_L-S_R}=4[4Em_nq^2+(m_\tau^2-q^2)(m_{\Lambda_c}^2-m_n^2-q^2)][2m_{\Lambda_c}^2(N_a\cdot p)-(N_a\cdot p')(m_{\Lambda_c}^2+m_n^2-q^2)]$$
$$\times\left[\frac{(m_{\Lambda_c}-m_n)f_0\tilde{h}_+}{m_cs_-}-\frac{(m_{\Lambda_c}+m_n)g_0h_+}{m_cs_+}\right]-\frac{16im_{\Lambda_c}(m_{\Lambda_c}^2-m_n^2)\varepsilon_{\{k\}\{k'\}\{N_a\}\{p\}}}{m_c}$$
$$\times(f_0h_\perp-g_0\tilde{h}_\perp)-4\{[4Em_nq^2+(m_\tau^2-q^2)(m_{\Lambda_c}^2-m_p^2-q^2)][(N_a\cdot p)(m_{\Lambda_c}^2-m_p^2+q^2)$$
$$+(N_a\cdot p')(m_n^2-m_{\Lambda_c}^2+q^2)]+(N_a\cdot k)(m_\tau^2+q^2)[m_{\Lambda_c}^4-2m_{\Lambda_c}^2(m_n^2+q^2)$$
$$+(m_n^2-q^2)^2]\}\left[\frac{m_{\Lambda_c}(m_{\Lambda_c}-m_n)^2f_0\tilde{h}_\perp}{m_cq^2s_-}-\frac{m_{\Lambda_c}(m_{\Lambda_c}+m_p)^2g_0h_\perp}{m_cq^2s_+}\right], \tag{C29}$$

$$\mathcal{A}^{h}_{S_L-S_R} = 0, \tag{C30}$$

where $\varepsilon_{\{k\}\{k'\}\{N_a\}\{p\}} \equiv \varepsilon_{\mu\nu\alpha\beta} k^{\mu} k'^{\nu} N_a^{\alpha} p^{\beta}$, with ε being a totally antisymmetric tensor. From the equations above, it is clear that $\mathcal{A}^{l,h}$ with the same subscripts are always real.

[1] J. P. Lees *et al.* (*BABAR* Collaboration), Phys. Rev. Lett. **109**, 101802 (2012).
[2] J. P. Lees *et al.* (*BABAR* Collaboration), Phys. Rev. D **88**, 072012 (2013).
[3] M. Huschle *et al.* (Belle Collaboration), Phys. Rev. D **92**, 072014 (2015).
[4] R. Aaij *et al.* (LHCb Collaboration), Phys. Rev. Lett. **115**, 111803 (2015); **115**, 159901(E) (2015).
[5] S. Hirose *et al.* (Belle Collaboration), Phys. Rev. Lett. **118**, 211801 (2017).
[6] S. Hirose *et al.* (Belle Collaboration), Phys. Rev. D **97**, 012004 (2018).
[7] R. Aaij *et al.* (LHCb Collaboration), Phys. Rev. Lett. **120**, 171802 (2018).
[8] R. Aaij *et al.* (LHCb Collaboration), Phys. Rev. D **97**, 072013 (2018).
[9] G. Caria *et al.* (Belle Collaboration), Phys. Rev. Lett. **124**, 161803 (2020).
[10] R. Aaij *et al.* (LHCb Collaboration), Phys. Rev. Lett. **131**, 111802 (2023).
[11] R. Aaij *et al.* (LHCb Collaboration), Phys. Rev. D **108**, 012018 (2023).
[12] S. Bifani, S. Descotes-Genon, A. Romero Vidal, and M.-H. Schune, J. Phys. G **46**, 023001 (2019).
[13] F. U. Bernlochner, M. F. Sevilla, D. J. Robinson, and G. Wormser, Rev. Mod. Phys. **94**, 015003 (2022).
[14] J. Albrecht, D. van Dyk, and C. Langenbruch, Prog. Part. Nucl. Phys. **120**, 103885 (2021).
[15] D. London and J. Matias, Annu. Rev. Nucl. Part. Sci. **72**, 37 (2022).
[16] P. Rubin *et al.* (CLEO Collaboration), Phys. Rev. D **73**, 112005 (2006).
[17] M. Ablikim *et al.* (BESIII Collaboration), Phys. Rev. Lett. **123**, 211802 (2019).
[18] R. Fleischer, R. Jaarsma, and G. Koole, Eur. Phys. J. C **80**, 153 (2020).
[19] D. Bečirević, F. Jaffredo, A. Peñuelas, and O. Sumensari, J. High Energy Phys. 05 (2021) 175.
[20] X. Leng, X.-L. Mu, Z.-T. Zou, and Y. Li, Chin. Phys. C **45**, 063107 (2021).
[21] P. Colangelo, F. De Fazio, and F. Loparco, Phys. Rev. D **103**, 075019 (2021).
[22] J. Fuentes-Martin, A. Greljo, J. Martin Camalich, and J. D. Ruiz-Alvarez, J. High Energy Phys. 11 (2020) 080.
[23] L. Allwicher, D. A. Faroughy, F. Jaffredo, O. Sumensari, and F. Wilsch, J. High Energy Phys. 03 (2023) 064.
[24] L.-F. Lai, X.-Q. Li, X.-S. Yan, and Y.-D. Yang, Phys. Rev. D **105**, 035007 (2022).
[25] L.-F. Lai, X.-Q. Li, X.-S. Yan, and Y.-D. Yang, Phys. Rev. D **105**, 115025 (2022).
[26] K. M. Graczyk, Nucl. Phys. **A748**, 313 (2005).
[27] A. Fatima, M. Sajjad Athar, and S. K. Singh, Phys. Rev. D **98**, 033005 (2018).
[28] K. M. Graczyk and B. E. Kowal, Phys. Rev. D **101**, 073002 (2020).
[29] J. E. Sobczyk, N. Rocco, A. Lovato, and J. Nieves, Phys. Rev. C **99**, 065503 (2019).
[30] S. Meinel, Phys. Rev. D **97**, 034511 (2018).
[31] N. Penalva, E. Hernández, and J. Nieves, Phys. Rev. D **101**, 113004 (2020).
[32] T. Feldmann and M. W. Y. Yip, Phys. Rev. D **85**, 014035 (2012); **86**, 079901(E) (2012).
[33] D. Das, Eur. Phys. J. C **78**, 230 (2018).
[34] A. Chodos, R. L. Jaffe, K. Johnson, C. B. Thorn, and V. F. Weisskopf, Phys. Rev. D **9**, 3471 (1974).
[35] A. Chodos, R. L. Jaffe, K. Johnson, and C. B. Thorn, Phys. Rev. D **10**, 2599 (1974).
[36] J. J. J. Kokkedee, *The Quark Model* (W. A. Benjamin, New York, 1969).
[37] M. A. Ivanov, V. E. Lyubovitskij, J. G. Korner, and P. Kroll, Phys. Rev. D **56**, 348 (1997).
[38] T. Branz, A. Faessler, T. Gutsche, M. A. Ivanov, J. G. Korner, and V. E. Lyubovitskij, Phys. Rev. D **81**, 034010 (2010).
[39] C. Bourrely, I. Caprini, and L. Lellouch, Phys. Rev. D **79**, 013008 (2009); **82**, 099902(E) (2010).
[40] G. De Lellis, P. Migliozzi, and P. Santorelli, Phys. Rep. **399**, 227 (2004); **411**, 323(E) (2005).
[41] Dune fluxes, https://home.fnal.gov/ ljf26/DUNEFluxes/.
[42] P. Machado, H. Schulz, and J. Turner, Phys. Rev. D **102**, 053010 (2020).
[43] R. Acciarri *et al.* (DUNE Collaboration), arXiv:1512.06148.
[44] M. S. Athar and S. K. Singh, *The Physics of Neutrino Interactions* (Cambridge University Press, Cambridge, England, 2020).
[45] A. Fatima, M. Sajjad Athar, and S. K. Singh, Phys. Rev. D **102**, 113009 (2020).
[46] A. Buras, *Gauge Theory of Weak Decays* (Cambridge University Press, Cambridge, England, 2020).
[47] R. L. Workman *et al.* (Particle Data Group), Prog. Theor. Exp. Phys. **2022**, 083C01 (2022).
[48] Y. Aoki *et al.* (Flavour Lattice Averaging Group (FLAG)), Eur. Phys. J. C **82**, 869 (2022).
[49] N. Carrasco *et al.*, Phys. Rev. D **91**, 054507 (2015).
[50] A. Bazavov *et al.*, Phys. Rev. D **98**, 074512 (2018).

[51] K. S. Kuzmin, V. V. Lyubushkin, and V. A. Naumov, Nucl. Phys. B, Proc. Suppl. **139**, 154 (2005).
[52] K. Hagiwara, K. Mawatari, and H. Yokoya, Nucl. Phys. **B668**, 364 (2003); **B701**, 405(E) (2004).
[53] J. E. Sobczyk, N. Rocco, and J. Nieves, Phys. Rev. C **100**, 035501 (2019).
[54] J. Nieves and J. E. Sobczyk, Ann. Phys. (Amsterdam) **383**, 455 (2017).
[55] R. Perez-Marcial, R. Huerta, A. Garcia, and M. Avila-Aoki, Phys. Rev. D **40**, 2955 (1989); **44**, 2203(E) (1991).
[56] M. Avila-Aoki, A. Garcia, R. Huerta, and R. Perez-Marcial, Phys. Rev. D **40**, 2944 (1989).
[57] T. Gutsche, M. A. Ivanov, J. G. Körner, V. E. Lyubovitskij, and P. Santorelli, Phys. Rev. D **90**, 114033 (2014); **94**, 059902(E) (2016).
[58] M. Ablikim *et al.* (BESIII Collaboration), Phys. Rev. Lett. **115**, 221805 (2015).
[59] M. Ablikim *et al.* (BESIII Collaboration), Phys. Lett. B **767**, 42 (2017).
[60] M. Ablikim *et al.* (BESIII Collaboration), Phys. Rev. Lett. **129**, 231803 (2022).
[61] M. A. Ivanov, J. G. Körner, and C.-T. Tran, Phys. Rev. D **95**, 036021 (2017).
[62] R. Alonso, J. Martin Camalich, and S. Westhoff, Phys. Rev. D **95**, 093006 (2017).
[63] P. Asadi, A. Hallin, J. Martin Camalich, D. Shih, and S. Westhoff, Phys. Rev. D **102**, 095028 (2020).
[64] Q.-Y. Hu, X.-Q. Li, Y.-D. Yang, and D.-H. Zheng, J. High Energy Phys. 02 (2021) 183.
[65] N. Penalva, E. Hernández, and J. Nieves, J. High Energy Phys. 06 (2021) 118.
[66] Q.-Y. Hu, X.-Q. Li, X.-L. Mu, Y.-D. Yang, and D.-H. Zheng, J. High Energy Phys. 06 (2021) 075.
[67] N. Penalva, E. Hernández, and J. Nieves, J. High Energy Phys. 10 (2021) 122.
[68] N. Penalva, N. Penalva, E. Hernández, E. Hernández, J. Nieves, and J. Nieves, J. High Energy Phys. 04 (2022) 026; 03 (2023) 11.
[69] X.-Q. Li, X. Xu, Y.-D. Yang, and D.-H. Zheng, J. High Energy Phys. 05 (2023) 173.
[70] E. Hernández, J. Nieves, F. Sánchez, and J. E. Sobczyk, Phys. Lett. B **829**, 137046 (2022).
[71] J. Isaacson, S. Höche, F. Siegert, and S. Wang, arXiv: 2303.08104.
[72] A. Khodjamirian, C. Klein, T. Mannel, and Y. M. Wang, J. High Energy Phys. 09 (2011) 106.
[73] C.-F. Li, Y.-L. Liu, K. Liu, C.-Y. Cui, and M.-Q. Huang, J. Phys. G **44**, 075006 (2017).
[74] S.-Q. Zhang and C.-F. Qiao, Phys. Rev. D **108**, 074017 (2023).
[75] C. Q. Geng, C.-W. Liu, and T.-H. Tsai, Phys. Rev. D **103**, 054018 (2021).
[76] C. Q. Geng, C.-C. Lih, C.-W. Liu, and T.-H. Tsai, Phys. Rev. D **101**, 094017 (2020).